Robust atmospheric river response to global warming in idealized and comprehensive climate models

Pengfei Zhang[1*], Gang Chen[2], Weiming Ma[2], Yi Ming[3], Zheng Wu[4]

1. Department of Meteorology and Atmospheric Sciences, Pennsylvania State University, University Park, PA 16802, USA

2. Department of Atmospheric and Oceanic Sciences, University of California, Los Angeles, CA 90095, USA

3. NOAA/Geophysical Fluid Dynamics Laboratory, Princeton, NJ 08542, USA

4. Institute for Atmospheric and Climate Science, ETH Zurich, Zurich, Switzerland

Revision, Jun. 2021

[*]Corresponding author: Pengfei Zhang (zpengfei1006@gmail.com, pfz5053@psu.edu)

Early Online Release: This preliminary version has been accepted for publication in *Journal of Climate*, may be fully cited, and has been assigned DOI 10.1175/JCLI-D-20-1005.1. The final typeset copyedited article will replace the EOR at the above DOI when it is published.

Abstract

Atmospheric rivers (ARs), narrow intense moisture transport, account for much of the poleward moisture transport in midlatitudes. While studies have characterized AR features and the associated hydrological impacts in a warming climate in observations and comprehensive climate models, the fundamental dynamics for changes in AR statistics (e.g., frequency, length, width) are not well understood. Here we investigate AR response to global warming with a combination of idealized and comprehensive climate models. To that end, we developed an idealized atmospheric GCM with Earth-like global circulation and hydrological cycle, in which water vapor and clouds are modeled as passive tracers with simple cloud microphysics and precipitation processes. Despite the simplicity of model physics, it reasonably reproduces observed dynamical structures for individual ARs, statistical characteristics of ARs, and spatial distributions of AR climatology. Under climate warming, the idealized model produces robust AR changes similar to CESM large ensemble simulations under RCP8.5, including AR size expansion, intensified landfall moisture transport, and an increased AR frequency, corroborating previously reported AR changes under global warming by climate models. In addition, the latitude of AR frequency maximum shifts poleward with climate warming. Further analysis suggests the thermodynamic effect (i.e., an increase in water vapor) dominates the AR statistics and frequency changes while both the dynamic and thermodynamic effects contribute to the AR poleward shift. These results demonstrate that AR changes in a warming climate can be understood as passive water vapor and cloud tracers regulated by large-scale atmospheric circulation, whereas convection and latent heat feedback are of secondary importance.

Accepted for publication in *Journal of Climate*. DOI 10.1175/JCLI-D-20-1005.1.

1. Introduction

Atmospheric rivers (ARs) are long, narrow corridors of synoptic horizontal water vapor transport in the midlatitude lower troposphere, accompanied with low-level jet streams ahead of the cold front of extratropical cyclones (e.g., Zhu and Newell 1998; Ralph et al. 2004; Neiman et al. 2008; Cordeira et al. 2013; Guan and Waliser 2015). These narrow corridors of concentrated moisture transport often originate from tropical oceans and carry large amounts of water vapor to the high latitudes, contributing 30-60% of the annual total precipitation to the west coasts of continents (e.g., Guan et al. 2010; Dettinger et al. 2011; Guan et al. 2012; Rutz and Steenburgh 2012; Viale et al. 2018). Too many, too strong, and/or long-lasting ARs, as well as a favorable antecedent soil moisture condition, bring extreme rainfall and floods to these regions (e.g., Dettinger 2006; Ralph et al. 2006; Stohl et al. 2008; Lavers et al. 2011; Neiman et al. 2011; Ralph et al. 2013; Konrad and Dettinger 2017; Paltan et al. 2017; Corringham et al. 2019; Ralph et al. 2019). ARs also breed snow accumulation and snowmelt events over both the Arctic and Antarctic (Gorodetskaya et al. 2014; Baggett et al. 2016; Hegyi and Taylor 2018; Mattingly et al. 2018; Wille et al. 2019), modulating the hydrological cycle in polar regions (Nash et al. 2018). An improved understanding of ARs in a warming climate is critical for predicting regional weather and hydrological extremes. In recent decades observations indicate that there are more landfalling ARs along with warming over the North Pacific (Gershunov et al. 2017). Under future warming, it is expected that ARs will become longer, wider and wetter (e.g., Espinoza et al. 2018). Both the intensity and the number of landfalling ARs and resultant heavy rainfall will increase in accordance with the projected warming (Lavers et al. 2015; Hagos et al. 2016; Curry et al. 2019; Gershunov et al. 2019; Huang et al. 2020; Ma et al. 2020b).

Given IVT consists of moisture and horizontal wind, the mechanisms for these AR changes in a warming climate can be roughly divided into two interrelated aspects (see reviews by Payne et al. 2020). The first mechanism is focused on the effects of robust thermodynamic characteristics of greenhouse gas increases on moisture. The Clausius-Clapeyron (CC) equation implies that the water-holding capability of the atmosphere increases with global warming. This is supported by many model studies suggested that the future changes of ARs are generally dominated by a uniform increase in atmospheric moisture and therefore the enhanced IVT in a warming climate (e.g., Gao et al. 2015, 2016; Lavers et al. 2015; Payne and Magnusdottir 2015; Warner et al. 2015). The other perspective is centered on the latitude of ARs due to the circulation response to global warming, termed as dynamic change. A poleward shift of ARs as the westerly jet shifts in a changing climate is found over North Atlantic and South Hemisphere (e.g., Gao et al. 2016; Ma et al. 2020a) while a small but robust reduction in IVT magnitude and an equatorward shift of ARs due to wind changes are found over North Pacific (e.g., Payne and Magnusdottir 2015; Gao et al. 2015; Shields and Kiehl 2016). In addition, ARs tend to occur with the extratropical cyclone development (Eiras-Barca et al. 2018; Zhang et al. 2019), which may be impeded by the reduction in the low-level baroclinic instability in a warmer climate, further increasing the complexity of AR response to global warming. Thus, the large uncertainty in midlatitude circulation changes, especially in comprehensive model simulation, can obfuscate a simple explanation of the AR dynamical response to global warming.

Climate models to date represent observed statistics of ARs relatively well while large regional biases still exist (e.g., Payne and Magnusdottir 2015; Guan and Waliser 2017 and the review by Waliser and Cordeira 2020). While the earlier studies have characterized the

AR features and associated hydrological impacts in a warming climate using comprehensive climate models, the fundamental dynamics (e.g., temperature gradient, baroclinic instability, eddy momentum flux, and eddy heat flux) for changes in AR statistics (e.g., frequency, length, width) are not well understood. Although simulating ARs as accurately as possible is vital to pursue robust projections of AR changes, the large uncertainty and complexity in the comprehensive climate model make it difficult to understand the fundamental dynamical processes in the AR response to a warming climate.

In this study, we take a different approach and examine the AR change in a warming climate using a combination of idealized and comprehensive climate models. Many idealized models have no explicit hydrological cycle (e.g., the dry dynamical core in Held and Suarez 1994) or unrealistic boundary conditions (e.g., the aquaplanet model in Neale and Hoskins 2000) and thus cannot simulate realistic spatial distributions of ARs. We developed a new idealized GCM with Earth-like global circulation with simple water vapor processes. Despite the simplicity of model physics, the idealized model produces robust AR changes under climate warming similar to a comprehensive model, improving our confidence in atmospheric moisture transport and the fundamentals of AR dynamics in a warming climate.

The paper is organized as follows. Section 2 describes the model setup of this new idealized model. The datasets used for model evaluation are also introduced in Section 2. Section 3 evaluates the performance of the idealized model in simulating the observed general circulation and hydrological cycle. The modeled ARs in the control run are evaluated with observations in Section 4. The circulation and AR responses to a warmer climate in the idealized model and CESM LENS are presented in Section 5.

2. Model setup and datasets

2.1. Model setup

In this study, a simple GCM is constructed to simulate reasonably accurate ARs and their changes in a warming climate. Unlike the comprehensive GCMs designed to model every observed detail as much as possible, simple models are designed to capture the fundamental physical processes only, and thus are valuable for understanding nature and are suitable for our goal. To simulate the ARs in a GCM with relatively simple physics but with atmospheric circulations close to the real atmosphere, we set up a dry atmospheric dynamical core by introducing Newtonian relaxation of temperature towards an equilibrium temperature that helps reproduce the observed climatology, and water vapor and cloud are implemented into the dry dynamical core as passive tracers, as described below.

We begin with the GFDL dry dynamical core (Held and Suarez 1994), which relaxes the temperature to a three-dimensional radiative equilibrium temperature field T_{eq} by Newtonian relaxation to mimic diabatic heating in the form of $(\partial T/\partial t) = -(T - T_{eq})/\tau$, where T is temperature and τ is a prescribed relaxation time scale given in the appendix of Jucker et al. (2014). The T_{eq} fields are determined individually for each month of the year and then linearly interpolated to daily values. To create a more Earth-like atmospheric circulation in the model, we employ the zonal asymmetric relaxation temperature field T_{eq} generated based on the mean state of the observation following (Wu and Reichler 2018), which was achieved through the iterative procedure described in Chang (2006). We simply describe the algorithm in Appendix A. The effect of seasonal variations in the mean state is examined by individually calculating for each month. While only the mean climate is the target of the

iteration process, transient eddies are created internally by the baroclinically unstable atmosphere. Eddy fluxes of momentum and energy highly resemble the observations with some slight differences in magnitude (Chang 2006, Wu and Reichler 2018), likely due to the close relationship between eddy statistics and mean climate. The actual Earth topography is employed in the model to further generate realistic planetary waves. There is no explicit boundary layer parameterization. The wind fields are damped by Rayleigh friction near the surface. With the above setting, an Earth-like atmospheric general circulation, including the stratospheric circulation and stationary planetary waves (Wu and Reichler 2018), is produced in this idealized model.

Given that the object of this study is ARs, which involves hydrological processes including moisture transport and precipitation as mentioned in the Introduction, a feasible technique to model the hydrological cycle is required. We achieve this by adopting a simple cloud physics in which the water vapor and cloud fraction are modeled as passive tracers, following Ming and Held (2018, MH18 hereafter). Here we simply summarize this cloud physics and describe a few technical differences of our work from MH18. In this simple cloud physics, there is no convective parameterization. Water vapor and cloud fraction are modeled as passive tracers, thus they do not affect the flow. There are three water tracers advected: specific humidity, liquid, and ice condensates. Surface evaporation is mimicked by nudging RH at the bottom layer to 100% with a time scale of 30min (as compared with RH below 850hPa is nudged in MH18). As in the GFDL HiRAM (Zhao et al. 2009), the large-scale cloud scheme diagnoses cloud fraction and condensation from grid-mean total water (water vapor and cloud condensates) using an assumed subgrid-scale distribution, which takes the form of a beta distribution with its width controlled by the grid-mean total water multiplied by a width

parameter, defined in Tompkins (2002). The beta distribution parameters are the same as MH18. We adopt a single-moment cloud microphysics developed by Rotstayn (1997) and Rotstayn et al. (2000), that has been successfully applied in GFDL AM2 and AM3. The main pathways for transformation between cloud condensates, precipitation formation, and re-evaporation of condensates, precipitation are involved. Same as MH18, this scheme assumes condensation (re-evaporation) not to generate condensational heating (cooling) and thus does not affect flow. No water vapor and cloud radiative effect is involved in this scheme either. Thus, water vapor and cloud are completely passive.

Given the model is a spectral core, a finite-volume gridpoint advection scheme, applicable to the gaussian grid, is used to advect the model's passive tracers. The horizontal tracer transport is computed using the finite-volume formulation (Lin and Rood 1996). This formulation has been examined by a study of tracer transport in baroclinic life cycle (Polvani and Esler 2007), an investigation of subtropical water vapor source (Galewsky et al. 2005), and isentropic mixing of tracers by large-scale atmospheric circulation (Chen and Plumb 2014). The reader is referred to MH18 for a more detailed exposition for the tracer advection algorithm.

Our model has 40 levels in the vertical. A sponge layer is employed near the model cap. The horizontal resolution is T42, with a resolution of about 2.8°×2.8°. We investigate the sensitivity of parameters for the calculation of cloud fraction and condensation, such as the width parameter for the tracer distribution that has been tested in MH18. The sensitivities in the vertical structure simulation of water vapor are reasonable and consistent with that in MH18 with a zonally symmetric circulation (figure not shown). More model evaluations for the simulations of cloud fraction, cloud water, and cloud ice will be presented in Section 3.

187

188 2.2. Datasets, method, and statistics

189 To evaluate the simulated circulation, hydrological cycle, and ARs, we compare the control
190 (Ctrl) run with ERA-Interim (ERAI) reanalysis (Dee et al. 2011). The variables from ERAI
191 have a horizontal resolution of 1.5°×1.5° and 37 levels in vertical. The daily data and the
192 long-term mean of 1979-2018 are used.

193

194 The outputs of 40 ensembles in the large ensemble simulation (LENS) based on CESM, a
195 comprehensive fully coupled climate model from NCAR, are employed (Kay et al. 2015).
196 Every member was under identical historical forcing before 2005 and RCP8.5 forcing after
197 that. We collect the daily data during 1979-2005 (27-year) in historical runs (Hist, hereafter)
198 and during 2074-2100 (27-year) in RCP8.5 runs (RCP8.5, hereafter). The projected AR
199 changes in CESM simulations are used to assess the AR response to climate warming in the
200 idealized model simulations.

201

202 The analysis in this study is based on the climatology of annual mean if no specific statement.
203 The pattern correlation coefficient (PCC) is employed to measure the pattern similarity
204 between the Ctrl run and observations. Vertical and latitudinal weights are considered, and
205 the global mean is removed before the calculation of PCC.

206

207 **3. Atmospheric circulation and hydrological cycle**

208 It is important to verify that this simple model is able to achieve a realistic atmospheric
209 circulation and hydrological cycle. We first conduct a control simulation (Ctrl run) based on
210 the model setup described above. The Ctrl run is integrated for 36 model years and the outputs

211 from the last 30 years are analyzed.

212

213 Starting with the zonal mean circulation, Figure 1a presents the zonal mean zonal wind (color)
214 and temperature (contour) in the Ctrl run. As expected, the modeled temperature field highly
215 resembles the ERAI as shown in Figure 1b, including the spatial pattern and the magnitude,
216 since the T_{eq} used to drive this model is produced to reproduce observations by an iterative
217 approach as described in Section 2.1. Specifically, the pattern correlation coefficient (PCC)
218 between the Ctrl and the ERAI is effectively 1.0, indicating the model recovers the spatial
219 pattern of temperature through the iterative process. Correspondingly, the zonal mean zonal
220 wind is well reproduced in this idealized model. The correlation coefficient for the zonal
221 mean zonal wind reaches 0.97. The westerly jet positions and their non-symmetric pattern in
222 two hemispheres, even in the stratosphere, are very close to that in the ERAI. These well-
223 reproduced zonal mean zonal wind patterns are mainly determined by the well-simulated
224 temperature field, especially over the extratropics where the thermal wind balance is
225 dominant. Figure 1c and d compare the mean meridional circulation and relative humidity in
226 the simple model and ERAI. In the tropics, the lack of convective scheme in our model leads
227 to an underestimation of the tropical convection in the simulation (determined by the
228 prescribed T_{eq}), therefore a weaker Hadley Cell (tropical convection) is produced in
229 comparison with the observation. However, the spatial pattern of the Hadley cell is well
230 captured in the simple model (PCC=0.93). Therefore, the vertical structure of the relative
231 humidity, such as the dry subtropics and wet high latitudes, shares similarity with that in
232 observation (PCC=0.91). It should be noted that the simulated relative humidity is generally
233 higher than that in ERAI, since we simply nudge the relative humidity to 100% at the bottom
234 level of the idealized model which exaggerates the wetness over the land area. In addition,

due to the lack of convection scheme and thus the weak vertical motions in the deep tropics, the model bias also lies in the vertical structure of RH (Fig.1cd). In the real atmosphere, the large values of low-level humidity and associated CAPE will trigger convective instability, which is generally treated by subgrid convective parameterizations in a comprehensive climate model, including the release of CAPE and mixing with drier environmental air. This setting prevents the excessive accumulation of moisture at the low level and the disappearance of the RH vertical gradient in the mid-to-upper troposphere in the tropics (Fig.1cd). Nevertheless, this simplification does not affect the simulation in the overall picture of the zonal mean structure of relative humidity which is controlled by the moisture transport associated with large-scale atmospheric circulation (Galewsky et al. 2005).

The moisture transport budget is $P - E = -\nabla \cdot Vq$ diagnosed in Figure 2 to assess the simulation of the hydrological cycle in the idealized model. The modeled precipitation minus evaporation (*P*-*E*) is balanced by the moisture transport $-\nabla \cdot Vq$. Compared to ERAI, while the moisture transport over the tropics and the subtropics of the South Hemisphere in the model is weaker due to the biases in the magnitude of the tropical convection, the water cycle over extratropical regions where most ARs occur is very close to the reanalysis data. The good simulation of the extratropical water vapor balance facilitates a reasonable simulation of ARs in this model (will be discussed later).

Figure 3 depicts the simulated cloud fields (cloud fraction, cloud liquid, and cloud ice) in the Ctrl run and ERAI reanalysis. The simulated clouds in the mid and low troposphere in the tropics are unrealistic due to the lack of a convection scheme, as we mentioned earlier. Thus, we consider the relevance of this model for the real atmosphere is confined to the extratropics.

Similar to MH18, the model is capable of qualitatively simulating some familiar aspects of the highly inhomogeneous cloud distribution over the tropical upper troposphere and extratropics compared with ERAI. Cloud fraction generally extends vertically through almost the entire troposphere in the extratropics, especially over the storm tracks where ARs occur frequently. The cloud fraction in the subtropical dry zones is also well reproduced in the model. Similar to ERAI, the transition from cloud liquid to ice in the Ctrl run follows the freezing line (Figure 3cdef).

4. Characteristics of Atmospheric Rivers

According to the above evaluation, the simple model used here is capable of reasonably modeling the realistic large-scale circulation and moisture transport, especially over the extratropical regions. We next further verify that this model is able to simulate ARs, including their fine-scale dynamical structure and climatological distribution. The AR detection method in Guan and Waliser (2015) is employed in this study. This AR detection algorithm is based on integrated water vapor transport (IVT) derived from specific humidity and wind fields at the pressure levels between 1000 and 300hPa inclusive for the idealized model and ERAI. For CESM LENS, IVT is calculated by vertically integrated specific humidity and horizontal winds from near the surface to 200mb because data at 1000 and 100hPa is not archived. The 85th percentile of IVT strength or 100 kg m^{-1} s^{-1}, whichever is greater, is chosen as the threshold for AR detection at each grid for each month. Since the 85th percentile IVT is used as a threshold most of the time, any bias in the IVT calculation will be implicitly accounted for when detecting ARs. Therefore, this AR detection algorithm is not sensitive to the ways how IVT is derived. Only objects with its meridional component of mean IVT greater than 50 kg m^{-1} s^{-1} are considered, given the notion that ARs transport

water vapor from low to high latitudes. For the detected object to be considered as AR, there should be less than half of the grid cells that have IVT deviating more than 45° from the object's mean IVT direction. In addition, the direction of mean IVT deviates from the overall orientation should be less than 45°. The overall orientation here is defined as the mean azimuth of the arc connecting the two end grid cells of AR's axis with the maximum great circle distance following Guan and Waliser (2015). In this algorithm, AR should be longer than 2000 km and with a length to width ratio of at least 2:1.

Figure 4 gives the spatial structure of a specific AR in the model and in the ERAI, respectively. We compose this figure following Ralph et al. (2017) and one can see that the modeled AR captures the key AR characteristics, i.e., a narrow, elongated, synoptic-scale jet of water vapor extending thousands of kilometers in length and an order of magnitude less in width. As shown in the vertical cross-section of ERAI (Figure 4d), the low-level moisture transport is concentrated in the bottom 3km of the atmosphere. While the low-level jet ahead of the cold front carries the vast majority of the horizontal water vapor transport, the cold upper-jet advects dry air aloft. Despite the coarse resolution and simple moist scheme, this coherent spatial structure is well reproduced in the idealized model (Figure 4c), indicating a major role of large-scale atmospheric circulation in the development of ARs through isentropic mixing of air mass and moisture (Chen and Plumb 2014).

The AR climatology simulated in this idealized model is further assessed. Figure 5 presents the climatologies of IVT and AR frequency. The strong moisture transport mainly occurs over the tropical trade wind belts (i.e., ITCZ), monsoon regions and midlatitude oceanic basins (Fig. 5b). Since there is no convective parameterization in the model, the ITCZ is

307 hardly simulated, while the water vapor transport over the Asian Monsoon region can be
308 reproduced mainly due to the topography effect. In contrast, the pattern of moisture transport
309 over the extratropics, especially over the midlatitude oceanic basins, where the storm tracks
310 and ARs are active, is well reproduced ($PCC_{extratropics}$=0.82), except that the values are lower
311 than the observation again due to the lack of convection scheme and thus no condensational
312 heating feedback in the model. In addition, the coarse resolution could contribute to this
313 underestimation as well. Given that ARs are defined with the threshold of 85th percentile
314 IVT, thus not sensitive to the climatological magnitude of IVT, the pattern of AR frequency
315 is well simulated in the model (PCC=0.95). In addition, the magnitude of the AR frequency
316 over the midlatitude ocean is in good agreement with that in the observation (8-14%).
317
318 Given the ARs are active at the midlatitudes as shown above, we calculate the zonally
319 integrated meridional IVT associated with AR transport and the AR zonal scale over 30°-
320 50°N(S) following Guan and Waliser (2015). The results show that the ARs account for 81%
321 (82%) of the total meridional IVT and 9% (11%) of the zonal circumference over 30°-50° in
322 the Northern (Southern) Hemisphere in the Ctrl run. The AR fractional IVT is slightly lower
323 than that in the observations, 85% (89%) of total meridional IVT, which could be due to the
324 idealized setting of excessive surface moisture over the land where the AR activity is much
325 less. The AR fractional zonal-scale in the idealized model matches the observation, 8% (11%)
326 of the zonal circumference, indicating that the idealized model relatively well captures the
327 key characteristic of ARs found in early studies that estimated ARs, while covering ~10% of
328 the Earth's circumference at midlatitudes, accounts for the majority of the total poleward
329 water vapor transport at these latitudes (e.g., Zhu and Newell 1998; Newman et al. 2012;
330 Guan and Waliser 2015).

Figure 6 shows the probability density function (PDF) of AR basic characteristics in Ctrl run and ERAI, including size (length and width), meridional range (lowest latitude and highest latitudes), direction of mean IVT and coherence of IVT direction, mean magnitude of IVT, landfall magnitude. Here, the coherence of the IVT direction of an AR event is measured by the fraction of AR grid cells with IVT directed within 45° of the mean AR IVT (Guan and Waliser 2015). For the AR size, the distribution of AR length is well reproduced in the idealized simulation, while the AR width in Ctrl is about 200km wider than that in the observation (Fig. 6ab). This biased PDF shift in the simulated AR width is likely due to the coarser spatial grids in the idealized model compared to 1.5°×1.5° in ERAI, since the coarse horizontal resolution of the model cannot capture the filamentation aspect of the ARs well (Guan and Waliser 2015). The PDFs of the highest and lowest latitude of ARs in each hemisphere, which measure the meridional range of AR activities, also match the observations (Fig.6cd). The PDFs of the direction of mean IVT and its coherence in the Ctrl run are well in agreement with the observation in both hemispheres (Fig. 6ef). For the magnitude of landfall IVT and the mean magnitude of IVT, although bias is found in the simulated PDFs, the basic shapes of the distribution are captured by the idealized model (Fig. 6gh). The too strong landfalling ARs in the idealized simulation is probably due to the setting of humidity in the model, in which the relative humidity is simply nudged to 100% at the lowest level without the moisture limitation over land. Overall, besides some biases in quantitative values of width and magnitude, the general AR characteristics are well simulated in the idealized model, further corroborating that the AR dynamics is dominated by large-scale atmospheric circulation and associated moisture transport.

In summary, the simple model used in this study is capable of simulating not only the large-scale circulation and hydrological cycle but also the 3-D spatial structure and statistical characteristics of the ARs with some quantitative biases. These results demonstrate the basic dynamics of ARs can be understood through the transport of passive water vapor and cloud tracers, indicating the important role of large-scale circulation and advection in the simulation of IVT and thus the AR activity.

5. AR response to global warming

5.1. Experimental design and the mean state response to climate warming

Since this idealized model is reliable for AR simulation as evaluated in the last section, we next explore the response of ARs to a changing climate in this simple model. A series of experiments with idealized warming (or cooling) forcing is conducted. The forcing employed in this study is a uniform temperature perturbation in the troposphere and a schematic diagram (Fig. 7a) shows the design for the vertical profile of the uniform, 4K for example, tropospheric warming (Trop4K), which is comparable to a ~4.4K warming on average by the end of 21 century in RCP8.5 scenario in CESM LENS simulations. Compared to the Ctrl run, a 4K warming is prescribed in T_{eq} fields at each grid below the tropopause (red segment). A linear transition zone is taken into account near the tropopause to mimic an uplifting tropopause induced by tropospheric warming with no change to tropospheric lapse rate. For each temperature profile for Trop4K forcing, the lapse rate in the transition zone is determined by the averaged lapse rate in the three layers below the tropopause in the Ctrl run, thus the thickness may vary from profile to profile. A similar approach was used in Lorenz and DeWeaver (2007) for a raised tropopause. The dotted green line in Fig.7a denotes the new tropopause for 4K warming. The actual temperature change for the 4K warming

379 experiment is shown in Figure 7b (color shading). More experiments demonstrate that the
380 results are not sensitive to the choice of the parameters to set up the transition zone (not
381 shown). Such a thermal forcing is designed to mimic the thermal effect of uniform SST
382 increase in aquaplanet simulations (e.g., Chen et al. 2013), with the effect of changes in lapse
383 rate excluded. Similarly, a series of experiments with a range of forcing, 2K tropospheric
384 warming, 2K and 4K tropospheric cooling, are conducted to explore the AR changes over a
385 range of climates. The transition zone for the tropospheric cooling forcing is determined
386 similarly as that in the warming forcing, except that the transition zone and the new
387 tropopause are below the tropopause in the Ctrl run. These perturbation experiments have
388 been run for 36 model years, respectively, and the last 30-year outputs are used for analysis,
389 same as the Ctrl run. The response is defined as the differences between the perturbation run
390 and the Ctrl run. The same IVT threshold, the 85th percentile of IVT in the reference state,
391 is used for AR detection in the perturbation scenarios.
392
393 We first show the responses of the zonal mean circulation to the tropospheric 4K warming
394 experiment (Trop4K) in Figure 8 (left column). The results are approximately opposite in
395 sign for the tropospheric 4K cooling experiments (Trop-4K) and thus are not shown here. To
396 further verify the model is able to simulate a reasonable response to tropospheric 4K warming,
397 we compared the responses in the idealized model to that in the comprehensive model
398 simulations, CESM LENS (right column of Fig. 8). The zonal mean results are also similar
399 to the atmospheric responses to 4K uniform SST increase in aquaplanet models (e.g., Chen
400 et al. 2013), which have an intermediate complexity in model physics between the idealized
401 model and CESM. The response in LENS/CESM is defined as the difference between the
402 climatologies of 2074-2100 in RCP8.5 and 1979-2005 in Hist. Compared to the tropospheric

403 4K warming in the idealized simulation, the global tropospheric temperature response is
404 about 4.4K in LENS/CESM. As a result of the uniform tropospheric 4K warming forcing, a
405 warmer troposphere can be seen in Fig. 8a. However, the pattern of temperature response is
406 not totally uniform, especially over extratropics, indicating the impact of the circulation
407 feedback. Although the projected deep tropical warming and polar amplification cannot be
408 fully represented, the uniform tropospheric warming still creates a temperature gradient
409 increasing at the upper troposphere over the subtropics to midlatitudes due to the slope in the
410 tropopause. Accordingly, consistent with the temperature changes and thermal wind balance,
411 the responses in the zonal mean zonal wind are characterized by a poleward shift in the
412 midlatitude westerly jet (more obvious in the South Hemisphere), with a large acceleration
413 near the subtropical tropopause (Fig. 8ac), resembling the zonal mean zonal wind responses
414 in the LENS/CESM (Fig. 8bd). The temperature gradient changes and jet shifts could
415 influence the Hadley Cell as well (see the review by Vallis et al. 2015). The response of the
416 mean meridional circulation to Trop4K warming shows a weaker Hadley cell, with a
417 poleward expansion in the Hadley cell and a poleward shift in the Ferrel cell (Fig. 8e) due to
418 the decrease of baroclinic instability and the eddy feedback, displaying the classic pattern of
419 the meridional circulation response to a warming climate, that has been found in the
420 comprehensive models (Fig. 8f) in many previous studies. This shift in atmospheric
421 circulation in response to uniform tropospheric warming in the presence of a sloping
422 tropopause is consistent with a recent study that quantifies a high sensitivity of the zonal jet
423 to changes to the upper-tropospheric temperature gradient (Chen et al. 2020).
424
425 Changes in zonal mean circulation certainly lead to distinct changes in water vapor and
426 hydrological cycle. The responses of relative humidity are characterized by wetness in the

stratosphere and dryness in the tropospheric extratropics (Fig.8g). The former is likely the result of increased water vapor entering the stratosphere in response to tropospheric warming and the latter indicates a larger increase in the saturation vapor pressure than the vapor pressure in a warming climate. These responses in relative humidity are generally in agreement with that in the RCP8.5/LENS except the differences over the upper tropical troposphere likely due to the lack of convective scheme (Fig. 8h). Previous studies (Wright et al. 2010) suggested that the spatial distribution of zonal mean relative humidity responses is largely dependent on circulation and transport changes, such as the poleward expansion of the Hadley Cell, poleward shift of the extratropical jets, and increase in the height of the tropopause as illustrated in previous sections. The tropospheric warming effects are also reflected in changes of precipitation minus evaporation (*P*-*E*, Fig. 9), a measure of the global water vapor budget. The responses roughly show a drying effect in the subtropical regions where mean $P\text{-}E<0$ and a wetting effect in the extratropics and tropics where mean $P\text{-}E>0$ (Fig. 9), a well-known thermodynamic mechanism for the hydrological cycle response to global warming (e.g., Chou and Neelin 2004; Held and Soden 2006). In addition, the magnitude of *P*-*E* changes over the extratropics in the idealized simulation is close to that in CESM LENS.

5.2. Response of ARs in climate warming

As discussed above, the changes of atmospheric circulation and hydrological cycle in the idealized model experiments resemble that in the comprehensive model simulations, paving the way to explore the response of ARs under a warming climate with a combination of the idealized and comprehensive model. Here we present the response of AR frequency in the Trop4K run in Figure 10a. The AR frequency increases over the mid-high latitude regions in

response to the tropospheric 4K warming, especially over the poleward side of its climatological maximum in the South Hemisphere in the Ctrl run. These more frequent AR activities in a warmer climate are highly consistent with those in the RCP8.5/CESM simulations (Fig. 10b) and many previous studies (see the review by Payne et al. 2020), confirming that the idealized model design is capable of simulating the AR response to global warming.

To explore the mechanisms of changes in ARs, we employ a simple scaling method developed in Ma et al. (2020) to separate the AR response due to the moisture change with climate warming (thermodynamic effect), i.e., Clausius-Clapeyron relation, and that due to the dynamical effect (wind changes). Note that our method rescales daily IVT in a warming climate by the change in climatological mean moisture, and then the same threshold can be used to compare different scenarios. We create two hypothetical scenarios of daily IVT for each perturbation run by a scaling method applying to specific humidity, given the moisture changes are expected to scale in line with CC. In the first scenario for the ARs with dynamic effect, the specific humidity at each time step, each pressure level, and each grid cell in the perturbation run is scaled with a factor of q_c/q_p, where $q_c(q_p)$ is the climatological specific humidity in the Ctrl (perturbation) run at the level and grid cell to which this factor applies. By scaling the data this way, the AR response due to specific humidity changes is removed in the hypothetical scenario. Then, the dynamic effect is isolated by contrasting this scaled case against the Ctrl run. Similarly, for the second hypothetical scenario of thermodynamic effect, the wind and specific humidity in Ctrl are used but the specific humidity in the Ctrl run is scaled with a factor of q_p/q_c so as to remove the dynamic response. The thermodynamic effect is the difference between the second hypothetical scenario and the Ctrl run. These two

components are linearly additive (see Fig.11e), indicating that the covariance of the two components is negligible.

Additionally, we also analyze the sensitivity of the thermodynamic component to local temperature changes (thermo_Local) versus global temperature changes (thermo_GlobalMean). This separates the nonlinear moisture dependence on temperature. That is, while the increase of saturation vapor pressure with temperature is commonly referred to as 7% K^{-1} warming, this rate is larger at lower temperatures (e.g., polar regions). Specifically, for the additional hypothetical scenario of thermo_GlobalMean, the wind and specific humidity in the Ctrl run are used but the specific humidity in the Ctrl run is scaled by a factor of $[q_p]/[q_c]$, where the [] denotes the global mean, and therefore the ARs with the thermodynamic effect due to the global mean change are detected. The difference between the thermodynamic effect and the Thermo_GlobalMean can be regarded as the Thermo_Local effect.

The AR frequency increases are mainly attributed to the thermodynamic effect (Fig. 11a), i.e., the moisture changes in line with CC, in which the thermo_GlobalMean dominates the magnitude changes over the midlatitudes (Fig. 11c). In contrast, the thermo_Local and dynamic effects contribute to the AR poleward shift (Fig.11bd). The thermo_Local is also characterized by a dipole structure in the midlatitude oceans (Fig. 11d), which is likely the imprint of the storm track shift in the tracer field of water vapor. We further quantify the contribution of dynamic and thermo_Local effects in Fig. 11f by presenting the zonal mean AR frequency. The dynamic effect leads to an AR decrease over the midlatitude and increase over the high latitude, contributing to the poleward shift of ARs. The contribution of

499 thermo_Local to the AR increases in high latitudes is comparable to or even larger than the
500 dynamic effect. This thermo_Local effect on a global scale has not been studied yest while
501 most previous studies attribute the AR poleward shift only to the wind changes focusing on
502 region of interest. In addition, the dynamic effect also results in an AR increase over the
503 subtropics of the North Hemisphere, suggesting the topographic effect in the asymmetric
504 responses of two hemispheres.
505
506 Next, we check the responses in the basic characteristics of ARs in Figure 6. Robust
507 responses are found in length, width, coherence of direction, and landfall magnitude, as
508 illustrated in Fig. 12. In response to the uniform tropospheric 4K warming, the ARs become
509 longer and wider, denoting larger ARs are expected under global warming according to the
510 same detection threshold (Fig. 12ac). It is worthy to note that the coherence of IVT direction
511 decreases along with the size increasing (Fig. 12e), given the detected ARs are larger
512 according to the same threshold and thus presenting a less organized feature. The intensity
513 of landfalling ARs is enhanced in a warmer climate (Fig. 12g), consistent with previous
514 studies (e.g., Lavers et al. 2015; Hagos et al. 2016; Espinoza et al. 2018; Curry et al. 2019;
515 Gershunov et al. 2019; Huang et al. 2020). These results in the idealized model are in
516 agreement with the responses in the RCP8.5 scenario in CESM LENS simulations with a
517 ~4.4K warming on average (Fig.12, right column). The consistency in the responses of AR
518 characteristics between the idealized model and comprehensive model further indicates that,
519 although there are some biases in the simulation of AR characteristics (e.g., width in Fig6b),
520 the idealized model is able to simulate the AR changes in a warming climate. The simplicity
521 of model physics in the idealized model demonstrates that the projected AR changes under
522 global warming can be understood as passive water vapor and cloud tracers without explicit

consideration of convections and associated latent heating feedback, and thus are not particularly sensitive to details of model physics. In other words, the dominant physical mechanism for atmospheric rivers is the mixing of air mass and moisture along isentropic surfaces associated with large-scale tropospheric weather systems (Chen and Plumb 2014), which also play a major role in the humidity structure of the atmosphere (Galewsky et al. 2005; Wright et al. 2010).

One advantage of the idealized model over the comprehensive model is to test the sensitivity of the response to climate forcing. Here we further investigate the AR changes among a range of climates (-4K, -2K, 0, 2K, 4K temperature forcing; See Tab. 1). The zonal means of the AR frequency in a series of experiments are shown in Figure 13a. The AR activities gradually become more frequent along linearly with the tropospheric temperature changes, while a clear poleward shift is found in the latitude of the AR frequency maximum, especially over the South Hemisphere. The increase of AR frequency over the South Hemisphere along with warming is larger than that in the North Hemisphere. This hemispheric asymmetry is enhanced along with the forcing magnitude. The poleward shift of the ARs and its hemispheric asymmetry in a warming climate is in agreement with that in the RCP8.5/CESM simulations (Fig. 13b). Observations also witnessed a poleward shift in AR in recent decades, with important implications for moisture transport into the Antarctic (Ma et al. 2020a). Interestingly, the increase of AR frequency in the Trop4K run is 48.1%, while a 50% increase is found in the RCP8.5/CESM simulation with a tropospheric 4.4K warming on average. Thus, we conclude that the shift and intensification of AR frequency in response to global warming in the idealized model experiments are comparable to those in the CESM simulation.

For the statistics of the basic characteristics of ARs, the PDFs present a monotonic change among a range of climates (Fig. 14). The PDFs of AR size tend to shift to the longer and wider sides in a warming world and to shift to the shorter and narrower sides in a cooling world according to the same detection threshold (Fig. 14ab). Along with the AR size expansion due to the monotonic temperature increases, the coherence of ARs is weakened monotonically (Fig.14c). The PDF of the magnitude of landfalling IVT tends to shift to the more intense side gradually along with temperature increases, indicating the amplified influence on the coastal region following further warming in the future. The line chart in each subplot of Fig. 14 explicitly shows the shifts of medians (gray line with colored stars) to their reference state (the median in Ctrl or Hist). Similar to the response in AR frequency, the change of the medians in simple model simulation Trop4K are quantitatively close to that in CESM LENS RCP8.5 with a tropospheric 4.4K warming on average (compare the red star and solid circle in each line chart in Fig. 14). The above results demonstrate that the responses of ARs in a warming climate, albeit with some biases, can be understood as passive water vapor and cloud tracers in a changing circulation. This simple physical setup helps to boost our confidence in the model projections of ARs in a warmer climate. Further, the contributions of dynamic and thermodynamic to the changes in AR characteristics are also shown in the line chart in each subplot (green and orange lines, respectively). It is clear that the thermodynamic response is dominant and the dynamic response can be ignored. These analyses indicate that the AR structure changes (e.g., larger size) in a warmer climate are mainly due to the higher moisture in a warmer climate that leads to more grids fulfilling the same detection threshold, while the response in the wind field contributes little to the AR structure changes. For the response of landfall IVT (Fig. 14d), the dynamic effect even weakens the landfalling ARs, i.e., the weaker velocity of midlatitude storms in a warmer

571 climate (e.g., Caballero and Hanley 2012), while the moisture carried by landfalling ARs
572 predominantly increases in a warming climate, and thus their total effect enhances the
573 landfalling ARs.
574
575 **6. Conclusions**
576 In this study, we have presented the statistics of atmospheric river response to global warming
577 in idealized and comprehensive climate models. In particular, we developed a new idealized
578 GCM with Earth-like global circulation and hydrological cycle to simulate the spatial
579 distribution of the ARs and their response to a warming climate. In this idealized model, the
580 mean temperature resembles the observations through relaxation to prescribed equilibrium
581 temperature with an iterative method (Chang 2006; Wu and Reichler 2018), and water vapor
582 and clouds are modeled as passive tracers with cloud microphysics and precipitation
583 processes but without cloud radiative effects or latent heat release (MH18). Despite the
584 simplicity of model physics, this idealized GCM produces qualitatively similar global
585 moisture transport, *P-E*, and cloud distributions as compared with observations; especially
586 over the extratropics, the model produces remarkable simulations in the dynamical structure
587 of individual ARs, the basic statistical characteristics of ARs and the realistic spatial
588 distributions of AR climatology. This idealized model under uniform tropospheric warming
589 projects robust AR changes in response to global warming similar to the CESM LENS
590 simulations under RCP8.5, including the AR size expansion according to the same detection
591 threshold, intensified landfall moisture transport magnitude, and an increase in AR frequency,
592 which is mainly attributed to the higher moisture with warmer climate (i.e., thermodynamic
593 effect), further improving our confidence in previously reported AR changes under global
594 warming (e.g., Lavers et al. 2015; Payne and Magnusdottir 2015; Warner et al. 2015; Gao et

595 al. 2016; Hagos et al. 2016; Gershunov et al. 2017; Espinoza et al. 2018; Curry et al. 2019).
596 In addition, the AR frequency shifts poleward with uniform tropospheric warming. We
597 further suggest that this poleward shift is attributed not only to the dynamic effect but also to
598 the thermodynamic effect due to the nonlinear moisture dependence on temperature, with a
599 larger increase in saturation vapor pressure with warming at lower temperatures (e.g., polar
600 regions). The contribution of the local nonlinear effect to the poleward shift in ARs has not
601 been studied yet. This poleward shift is more notable in the South Hemisphere, where
602 observations saw a poleward shift in AR in recent decades, with important implications for
603 the moisture transport into the Antarctic (Ma et al. 2020a).
604
605 These results demonstrate, despite their fine-scale structures, the basic dynamics of ARs in a
606 warming climate can be understood as passive water vapor and cloud tracers without explicit
607 consideration of convections and associated latent heat feedback. In other words, the
608 dominant physical mechanism for atmospheric rivers is the mixing of air mass and moisture
609 along isentropic surfaces associated with large-scale tropospheric weather systems (Chen and
610 Plumb 2014), which also play a major role in the humidity structure of the atmosphere
611 (Galewsky et al. 2005; Wright et al. 2010). This may be a little counterintuitive as latent heat
612 release is often considered as a major source of energy that reinforces the synoptic storm
613 associated with an AR. This may be explained by a recent study on midlatitude extreme
614 precipitation, in which the latent heat feedback is largely canceled by the increased
615 stratification in a warming climate (Li and O'Gorman 2020).
616
617 Although the idealized model simulates the ARs and their responses in changing climate well,
618 care must be taken in generalizing this simple model to some studies of ARs in the real

619 climate. For example, given some tropical factors, such as Madden-Julian Oscillation (MJO)
620 and El Nino-Southern Oscillation (ENSO), could influence extratropical ARs through
621 atmospheric teleconnections (Guan et al. 2012; Guan and Waliser 2015; Mundhenk et al.
622 2016), the biased simulation over the tropics in the idealized model may limit its capability
623 to model the variability of ARs. In addition, the modeled landfalling ARs are too strong as
624 compared to observations, because of the excessive moisture over the land simulated by the
625 model in which the relative humidity is simply nudged to 100% at the lowest model level. A
626 more realistic evaporation scheme with realistic land-sea contrast is warranted to describe
627 better the landfalling ARs and their impact on the coastal regions.
628
629 Finally, this idealized model provides a new tool for understanding Earth-like global
630 circulation and hydrological cycle on regional scales. Our study has demonstrated that the
631 idealized model can capture many features of atmospheric general circulation, midlatitude
632 storms, and moisture transport in a warming climate. Many idealized models have no explicit
633 hydrological cycle (e.g., Held and Suarez 1994) or unrealistic boundary conditions (e.g.,
634 Neale and Hoskins 2000) and thus cannot simulate realistic spatial distributions of ARs. The
635 new idealized model developed in this study overcomes these limitations and reproduces
636 individual ARs and their climatology well, and thus helps improve our confidence in regional
637 atmospheric moisture transport and AR dynamics in a warming climate.
638
639 **Appendix A:**
640 The model is supposed to reproduce a temperature field similar to a given reference
641 temperature climatology T_R. Here, T_R is the mean state of the MERRA2 in 1980-2015 (Wu
642 and Reichler 2018). For an iteration step *(i)*, a model run forced with a $T_{eq}(i)$ produces a time-

mean output temperature field $\bar{T}(i)$. Then we calculate the difference between $\bar{T}(i)$ and T_R and define $T_{eq}(i+1)$ as

$$T_{eq}(i+1) = T_{eq}(i) - \alpha(\bar{T}(i) - T_R) \qquad (1)$$

to yield $\bar{T}(i+1)$ closer to T_R. $\alpha = 2/3$ is used here following Chang (2006) to avoid overshooting the optimal T_{eq}. Equation (1) is then iterated until $T_{eq}(n)$ that yields a $\bar{T}(n)$ sufficiently close to T_R is generated.

Acknowledgement: We thank Dr. Bin Guan from JPL and Dr. Xingying Huang from NCAR for helpful discussion. We thank the three reviewers for their helpful suggestions. We would like to acknowledge high-performance computing support from Cheyenne (doi:10.5065/D6RX99HX) provided by NCAR's Computational and Information Systems Laboratory, sponsored by the NSF. P.Z., G.C., and W.M. were funded by the NSF (AGS-1742178 and AGS-1832842).

References:

Baggett, C., S. Lee, and S. Feldstein, 2016: An Investigation of the Presence of Atmospheric Rivers over the North Pacific during Planetary-Scale Wave Life Cycles and Their Role in Arctic Warming. *J. Atmos. Sci.*, **73**, 4329–4347, https://doi.org/10.1175/JAS-D-16-0033.1.

Caballero, R., & Hanley, J. (2012). Midlatitude Eddies, Storm-Track Diffusivity, and Poleward Moisture Transport in Warm Climates, *Journal of the Atmospheric Sciences*, 69(11), 3237-3250.

Chang, E. K. M., 2006: An Idealized Nonlinear Model of the Northern Hemisphere Winter Storm Tracks. *J. Atmos. Sci.*, **63**, 1818–1839, https://doi.org/10.1175/JAS3726.1.

Chen, G., and A. Plumb, 2014: Effective Isentropic Diffusivity of Tropospheric Transport. *Journal of Atmospheric Sciences*, **71**, 3499–3520, https://doi.org/10.1175/JAS-D-13-0333.1.

——, J. Lu, and L. Sun, 2013: Delineating the Eddy–Zonal Flow Interaction in the

Accepted for publication in *Journal of Climate*. DOI:10.1175/JCLI-D-20-1005.1.

Atmospheric Circulation Response to Climate Forcing: Uniform SST Warming in an Idealized Aquaplanet Model. *J. Atmos. Sci.*, **70**, 2214–2233, https://doi.org/10.1175/jas-d-12-0248.1.

——, P. Zhang, and J. Lu, 2020: Sensitivity of the Latitude of the Westerly Jet Stream to Climate Forcing. *Geophys. Res. Lett.*, **47**, e2019GL086563, https://doi.org/10.1029/2019gl086563.

Chou, C., and J. D. Neelin, 2004: Mechanisms of Global Warming Impacts on Regional Tropical Precipitation. *J. Climate*, **17**, 2688–2701, https://doi.org/10.1175/1520-0442(2004)017<2688:MOGWIO>2.0.CO;2.

Cordeira, J. M., F. M. Ralph, and B. J. Moore, 2013: The Development and Evolution of Two Atmospheric Rivers in Proximity to Western North Pacific Tropical Cyclones in October 2010. *Monthly Weather Review*, **141**, 4234–4255, https://doi.org/10.1175/MWR-D-13-00019.1.

Corringham, T. W., F. M. Ralph, A. Gershunov, D. R. Cayan, and C. A. Talbot, 2019: Atmospheric rivers drive flood damages in the western United States. *Science Advances*, **5**, eaax4631, https://doi.org/10.1126/sciadv.aax4631.

Curry, C. L., S. U. Islam, F. W. Zwiers, and S. J. Déry, 2019: Atmospheric Rivers Increase Future Flood Risk in Western Canada's Largest Pacific River. *Geophysical Research Letters*, **46**, 1651–1661, https://doi.org/10.1029/2018GL080720.

Dee, D. P., and Coauthors, 2011: The ERA-Interim reanalysis: configuration and performance of the data assimilation system. *Q. J. Royal Meteorol. Soc*, **137**, 553–597, https://doi.org/10.1002/qj.828.

Dettinger, M. D., 2006: *Fifty-two years of pineapple-express storms across the West Coast of North America*. California Energy Commission, http://pubs.er.usgs.gov/publication/70175879 (Accessed October 7, 2020).

Dettinger, M. D., F. M. Ralph, T. Das, P. J. Neiman, and D. R. Cayan, 2011: Atmospheric Rivers, Floods and the Water Resources of California. *Water*, **3**, 445–478, https://doi.org/10.3390/w3020445.

Eiras-Barca, J., A. M. Ramos, J. G. Pinto, R. M. Trigo, M. L. R. Liberato, and G. Miguez-Macho, 2018: The concurrence of atmospheric rivers and explosive cyclogenesis in the North Atlantic and North Pacific basins. *Earth System Dynamics*, **9**, 91–102, https://doi.org/10.5194/esd-9-91-2018.

Espinoza, V., D. E. Waliser, B. Guan, D. A. Lavers, and F. M. Ralph, 2018: Global Analysis of Climate Change Projection Effects on Atmospheric Rivers. *Geophysical Research Letters*, **45**, 4299–4308, https://doi.org/10.1029/2017GL076968.

Galewsky, J., A. Sobel, and I. Held, 2005: Diagnosis of Subtropical Humidity Dynamics Using Tracers of Last Saturation. *J. Atmos. Sci.*, **62**, 3353–3367,

https://doi.org/10.1175/JAS3533.1.

Gao, Y., J. Lu, L. R. Leung, Q. Yang, S. Hagos, and Y. Qian, 2015: Dynamical and thermodynamical modulations on future changes of landfalling atmospheric rivers over western North America. *Geophys. Res. Lett.*, **42**, 7179–7186, https://doi.org/10.1002/2015gl065435.

——, ——, and ——, 2016: Uncertainties in Projecting Future Changes in Atmospheric Rivers and Their Impacts on Heavy Precipitation over Europe. *J. Clim.*, **29**, 6711–6726, https://doi.org/10.1175/jcli-d-16-0088.1.

Gershunov, A., T. Shulgina, F. M. Ralph, D. A. Lavers, and J. J. Rutz, 2017: Assessing the climate-scale variability of atmospheric rivers affecting western North America. *Geophysical Research Letters*, **44**, 7900–7908, https://doi.org/10.1002/2017GL074175.

——, and Coauthors, 2019: Precipitation regime change in Western North America: The role of Atmospheric Rivers. *Scientific Reports*, **9**, 9944, https://doi.org/10.1038/s41598-019-46169-w.

Gorodetskaya, I. V., M. Tsukernik, K. Claes, M. F. Ralph, W. D. Neff, and N. P. M. V. Lipzig, 2014: The role of atmospheric rivers in anomalous snow accumulation in East Antarctica. *Geophysical Research Letters*, **41**, 6199–6206, https://doi.org/10.1002/2014GL060881.

Guan, B., and D. E. Waliser, 2015: Detection of atmospheric rivers: Evaluation and application of an algorithm for global studies. *J. Geophys. Res.*, **120**, 12514–12535, https://doi.org/10.1002/2015jd024257.

——, and ——, 2017: Atmospheric rivers in 20 year weather and climate simulations: A multimodel, global evaluation. *Journal of Geophysical Research: Atmospheres*, **122**, 5556–5581, https://doi.org/10.1002/2016JD026174.

——, N. P. Molotch, D. E. Waliser, E. J. Fetzer, and P. J. Neiman, 2010: Extreme snowfall events linked to atmospheric rivers and surface air temperature via satellite measurements. *Geophysical Research Letters*, **37**, https://doi.org/10.1029/2010GL044696.

——, D. E. Waliser, N. P. Molotch, E. J. Fetzer, and P. J. Neiman, 2012: Does the Madden–Julian Oscillation Influence Wintertime Atmospheric Rivers and Snowpack in the Sierra Nevada? *Mon. Wea. Rev.*, **140**, 325–342, https://doi.org/10.1175/MWR-D-11-00087.1.

Hagos, S. M., L. R. Leung, J.-H. Yoon, J. Lu, and Y. Gao, 2016: A projection of changes in landfalling atmospheric river frequency and extreme precipitation over western North America from the Large Ensemble CESM simulations. *Geophysical Research Letters*, **43**, 1357–1363, https://doi.org/10.1002/2015GL067392.

Accepted for publication in *Journal of Climate*. DOI:10.1175/JCLI-D-20-1005.1.

745 Hegyi, B. M., and P. C. Taylor, 2018: The Unprecedented 2016–2017 Arctic Sea Ice Growth
746 Season: The Crucial Role of Atmospheric Rivers and Longwave Fluxes. *Geophysical*
747 *Research Letters*, **45**, 5204–5212, https://doi.org/10.1029/2017GL076717.

748 Held, I. M., and M. J. Suarez, 1994: A Proposal for the Intercomparison of the Dynamical
749 Cores of Atmospheric General Circulation Models. *Bull. Am. Meteorol. Soc.*, **75**,
750 1825–1830, https://doi.org/doi:10.1175/1520-
751 0477(1994)075<1825:APFTIO>2.0.CO;2.

752 ——, and B. J. Soden, 2006: Robust Responses of the Hydrological Cycle to Global
753 Warming. *J. Clim.*, **19**, 5686–5699, https://doi.org/10.1175/jcli3990.1.

754 Huang, X., D. L. Swain, and A. D. Hall, 2020: Future precipitation increase from very high
755 resolution ensemble downscaling of extreme atmospheric river storms in California.
756 *Science Advances*, **6**, eaba1323, https://doi.org/10.1126/sciadv.aba1323.

757 Jucker, M., S. Fueglistaler, and G. K. Vallis, 2014: Stratospheric sudden warmings in an
758 idealized GCM. *Journal of Geophysical Research: Atmospheres*, **119**, 11,054-11,064,
759 https://doi.org/10.1002/2014JD022170.

760 Kay, J. E., and Coauthors, 2015: The Community Earth System Model (CESM) Large
761 Ensemble Project: A Community Resource for Studying Climate Change in the
762 Presence of Internal Climate Variability. *Bull. Am. Meteorol. Soc.*, **96**, 1333–1349,
763 https://doi.org/10.1175/bams-d-13-00255.1.

764 Konrad, C. P., and M. D. Dettinger, 2017: Flood Runoff in Relation to Water Vapor
765 Transport by Atmospheric Rivers Over the Western United States, 1949–2015.
766 *Geophysical Research Letters*, **44**, 11,456-11,462,
767 https://doi.org/10.1002/2017GL075399.

768 Lavers, D. A., R. P. Allan, E. F. Wood, G. Villarini, D. J. Brayshaw, and A. J. Wade, 2011:
769 Winter floods in Britain are connected to atmospheric rivers. *Geophysical Research*
770 *Letters*, **38**, https://doi.org/10.1029/2011GL049783.

771 ——, F. M. Ralph, D. E. Waliser, A. Gershunov, and M. D. Dettinger, 2015: Climate change
772 intensification of horizontal water vapor transport in CMIP5. *Geophysical Research*
773 *Letters*, **42**, 5617–5625, https://doi.org/10.1002/2015GL064672.

774 Li, Z., and P. A. O'Gorman, 2020: Response of Vertical Velocities in Extratropical
775 Precipitation Extremes to Climate Change. *Journal of Climate*, **33**, 7125–7139,
776 https://doi.org/10.1175/JCLI-D-19-0766.1.

777 Lin, S.-J., and R. B. Rood, 1996: Multidimensional Flux-Form Semi-Lagrangian Transport
778 Schemes. *Mon. Wea. Rev.*, **124**, 2046–2070, https://doi.org/10.1175/1520-
779 0493(1996)124<2046:MFFSLT>2.0.CO;2.

780 Lorenz, D. J., and E. T. DeWeaver, 2007: Tropopause height and zonal wind response to
781 global warming in the IPCC scenario integrations. *J. Geophys. Res.*, **112**,

https://doi.org/10.1029/2006jd008087.

Ma, W., G. Chen, and B. Guan, 2020a: Poleward Shift of Atmospheric Rivers in the Southern Hemisphere in Recent Decades. *Geophysical Research Letters*, **47**, e2020GL089934, https://doi.org/10.1029/2020GL089934.

——, J. Norris, and G. Chen, 2020b: Projected Changes to Extreme Precipitation Along North American West Coast From the CESM Large Ensemble. *Geophysical Research Letters*, **47**, e2019GL086038, https://doi.org/10.1029/2019GL086038.

Mattingly, K. S., T. L. Mote, and X. Fettweis, 2018: Atmospheric River Impacts on Greenland Ice Sheet Surface Mass Balance. *Journal of Geophysical Research: Atmospheres*, **123**, 8538–8560, https://doi.org/10.1029/2018JD028714.

Ming, Y., and I. M. Held, 2018: Modeling Water Vapor and Clouds as Passive Tracers in an Idealized GCM. *J. Clim.*, **31**, 775–786, https://doi.org/10.1175/jcli-d-16-0812.1.

Mundhenk, B. D., E. A. Barnes, and E. D. Maloney, 2016: All-Season Climatology and Variability of Atmospheric River Frequencies over the North Pacific. *Journal of Climate*, **29**, 4885–4903, https://doi.org/10.1175/JCLI-D-15-0655.1.

Nash, D., D. Waliser, B. Guan, H. Ye, and F. M. Ralph, 2018: The Role of Atmospheric Rivers in Extratropical and Polar Hydroclimate. *Journal of Geophysical Research: Atmospheres*, **123**, 6804–6821, https://doi.org/10.1029/2017JD028130.

Neale, R. B., and B. J. Hoskins, 2000: A standard test for AGCMs including their physical parametrizations: I: the proposal. *Atmospheric Science Letters*, **1**, 101–107, https://doi.org/10.1006/asle.2000.0022.

Neiman, P. J., F. M. Ralph, G. A. Wick, J. D. Lundquist, and M. D. Dettinger, 2008: Meteorological Characteristics and Overland Precipitation Impacts of Atmospheric Rivers Affecting the West Coast of North America Based on Eight Years of SSM/I Satellite Observations. *Journal of Hydrometeorology*, **9**, 22–47, https://doi.org/10.1175/2007JHM855.1.

——, L. J. Schick, F. M. Ralph, M. Hughes, and G. A. Wick, 2011: Flooding in Western Washington: The Connection to Atmospheric Rivers. *J. Hydrometeor.*, **12**, 1337–1358, https://doi.org/10.1175/2011JHM1358.1.

Newman, M., G. N. Kiladis, K. M. Weickmann, F. M. Ralph, and P. D. Sardeshmukh, 2012: Relative Contributions of Synoptic and Low-Frequency Eddies to Time-Mean Atmospheric Moisture Transport, Including the Role of Atmospheric Rivers. *J. Climate*, **25**, 7341–7361, https://doi.org/10.1175/JCLI-D-11-00665.1.

Paltan, H., D. Waliser, W. H. Lim, B. Guan, D. Yamazaki, R. Pant, and S. Dadson, 2017: Global Floods and Water Availability Driven by Atmospheric Rivers. *Geophysical Research Letters*, **44**, 10,387-10,395, https://doi.org/10.1002/2017GL074882.

Payne, A. E., and G. Magnusdottir, 2015: An evaluation of atmospheric rivers over the North

Pacific in CMIP5 and their response to warming under RCP 8.5. *Journal of Geophysical Research: Atmospheres*, **120**, 11,173-11,190, https://doi.org/10.1002/2015JD023586.

——, and Coauthors, 2020: Responses and impacts of atmospheric rivers to climate change. *Nature Reviews Earth & Environment*, **1**, 143–157, https://doi.org/10.1038/s43017-020-0030-5.

Polvani, L. M., and J. G. Esler, 2007: Transport and mixing of chemical air masses in idealized baroclinic life cycles. *Journal of Geophysical Research: Atmospheres*, **112**, https://doi.org/10.1029/2007JD008555.

Ralph, F. M., P. J. Neiman, and G. A. Wick, 2004: Satellite and CALJET Aircraft Observations of Atmospheric Rivers over the Eastern North Pacific Ocean during the Winter of 1997/98. *Monthly Weather Review*, **132**, 1721–1745, https://doi.org/10.1175/1520-0493(2004)132<1721:SACAOO>2.0.CO;2.

——, ——, ——, S. I. Gutman, M. D. Dettinger, D. R. Cayan, and A. B. White, 2006: Flooding on California's Russian River: Role of atmospheric rivers. *Geophysical Research Letters*, **33**, https://doi.org/10.1029/2006GL026689.

Ralph, F. M., T. Coleman, P. J. Neiman, R. J. Zamora, and M. D. Dettinger, 2013: Observed Impacts of Duration and Seasonality of Atmospheric-River Landfalls on Soil Moisture and Runoff in Coastal Northern California. *Journal of Hydrometeorology*, **14**, 443–459, https://doi.org/10.1175/JHM-D-12-076.1.

——, and Coauthors, 2017: Dropsonde Observations of Total Integrated Water Vapor Transport within North Pacific Atmospheric Rivers. *Journal of Hydrometeorology*, **18**, 2577–2596, https://doi.org/10.1175/jhm-d-17-0036.1.

Ralph, F. M., J. J. Rutz, J. M. Cordeira, M. Dettinger, M. Anderson, D. Reynolds, L. J. Schick, and C. Smallcomb, 2019: A Scale to Characterize the Strength and Impacts of Atmospheric Rivers. *Bull. Amer. Meteor. Soc.*, **100**, 269–289, https://doi.org/10.1175/BAMS-D-18-0023.1.

Rotstayn, L. D., 1997: A physically based scheme for the treatment of stratiform clouds and precipitation in large-scale models. I: Description and evaluation of the microphysical processes. *Quarterly Journal of the Royal Meteorological Society*, **123**, 1227–1282, https://doi.org/10.1002/qj.49712354106.

——, B. F. Ryan, and J. J. Katzfey, 2000: A Scheme for Calculation of the Liquid Fraction in Mixed-Phase Stratiform Clouds in Large-Scale Models. *Mon. Wea. Rev.*, **128**, 1070–1088, https://doi.org/10.1175/1520-0493(2000)128<1070:ASFCOT>2.0.CO;2.

Rutz, J. J., and W. J. Steenburgh, 2012: Quantifying the role of atmospheric rivers in the interior western United States. *Atmospheric Science Letters*, **13**, 257–261, https://doi.org/10.1002/asl.392.

Shields, C. A., and J. T. Kiehl, 2016: Atmospheric river landfall-latitude changes in future climate simulations. *Geophysical Research Letters*, **43**, 8775–8782, https://doi.org/10.1002/2016GL070470.

Stohl, A., C. Forster, and H. Sodemann, 2008: Remote sources of water vapor forming precipitation on the Norwegian west coast at 60°N–a tale of hurricanes and an atmospheric river. *Journal of Geophysical Research: Atmospheres*, **113**, https://doi.org/10.1029/2007JD009006.

Tompkins, A. M., 2002: A Prognostic Parameterization for the Subgrid-Scale Variability of Water Vapor and Clouds in Large-Scale Models and Its Use to Diagnose Cloud Cover. *J. Atmos. Sci.*, **59**, 1917–1942, https://doi.org/10.1175/1520-0469(2002)059<1917:APPFTS>2.0.CO;2.

Vallis, G. K., P. Zurita-Gotor, C. Cairns, and J. Kidston, 2015: Response of the large-scale structure of the atmosphere to global warming. *Q. J. Royal Meteorol. Soc*, **141**, 1479–1501, https://doi.org/10.1002/qj.2456.

Viale, M., R. Valenzuela, R. D. Garreaud, and F. M. Ralph, 2018: Impacts of Atmospheric Rivers on Precipitation in Southern South America. *J. Hydrometeor.*, **19**, 1671–1687, https://doi.org/10.1175/JHM-D-18-0006.1.

Waliser, D. E., and J. M. Cordeira, 2020: Atmospheric River Modeling: Forecasts, Climate Simulations, and Climate Projections. *Atmospheric Rivers*, F.M. Ralph, M.D. Dettinger, J.J. Rutz, and D.E. Waliser, Eds., Springer International Publishing, 179–199.

Warner, M. D., C. F. Mass, and E. P. Salathé, 2015: Changes in Winter Atmospheric Rivers along the North American West Coast in CMIP5 Climate Models. *J. Hydrometeor.*, **16**, 118–128, https://doi.org/10.1175/JHM-D-14-0080.1.

Wille, J. D., V. Favier, A. Dufour, I. V. Gorodetskaya, J. Turner, C. Agosta, and F. Codron, 2019: West Antarctic surface melt triggered by atmospheric rivers. *Nature Geoscience*, **12**, 911–916, https://doi.org/10.1038/s41561-019-0460-1.

Wright, J. S., A. Sobel, and J. Galewsky, 2010: Diagnosis of Zonal Mean Relative Humidity Changes in a Warmer Climate. *J. Clim.*, **23**, 4556–4569, https://doi.org/10.1175/2010jcli3488.1.

Wu, Z., and T. Reichler, 2018: Towards a More Earth-Like Circulation in Idealized Models. *J. Adv. Model Earth Syst.*, **10**, 1458–1469, https://doi.org/10.1029/2018ms001356.

Zhang, Z., F. M. Ralph, and M. Zheng, 2019: The Relationship Between Extratropical Cyclone Strength and Atmospheric River Intensity and Position. *Geophysical Research Letters*, **46**, 1814–1823, https://doi.org/10.1029/2018GL079071.

Zhao, M., I. M. Held, S.-J. Lin, and G. A. Vecchi, 2009: Simulations of Global Hurricane Climatology, Interannual Variability, and Response to Global Warming Using a 50-

Accepted for publication in *Journal of Climate*. DOI 10.1175/JCLI-D-20-1005.1.

km Resolution GCM. *J. Climate*, **22**, 6653–6678, https://doi.org/10.1175/2009JCLI3049.1.

Zhu, Y., and R. E. Newell, 1998: A Proposed Algorithm for Moisture Fluxes from Atmospheric Rivers. *Monthly Weather Review*, **126**, 725–735, https://doi.org/10.1175/1520-0493(1998)126<0725:apafmf>2.0.co;2.

Figure list

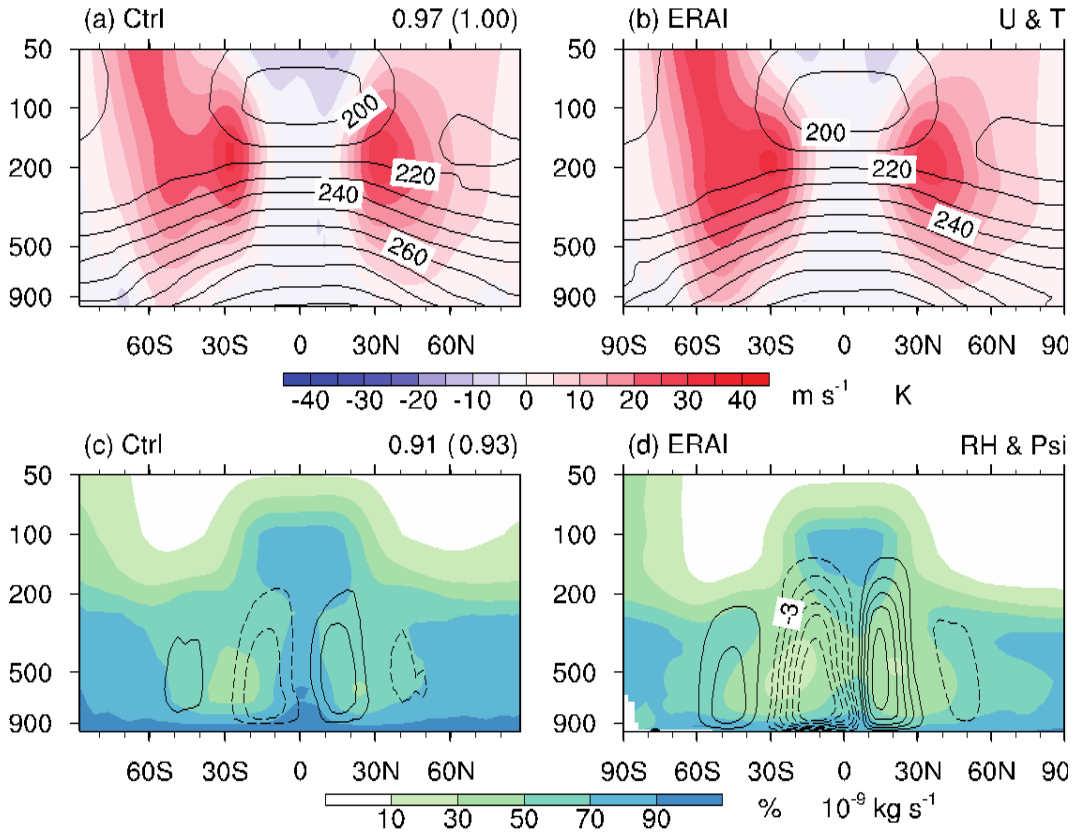

Fig.1 Zonal mean zonal wind, temperature, relative humidity and mean meridional circulation in the idealized model and observations. (a-b) Zonal mean zonal wind (color shading, m s^{-1}) and temperature (contour, K) in Ctrl run and ERAI. (c-d) Zonal mean relative humidity (Units: %) and meridional stream function (interval is 1.5×10^{-9} kg s^{-1}) simulated in Ctrl run and ERA. The value 0.97(~1.0) at the upper right of (a) is the pattern correlation coefficients between Ctrl and ERAI for zonal mean zonal wind (zonal mean temperature). The value 0.91(0.93) in (c) is that for RH (meridional stream function) between Ctrl and ERAI.

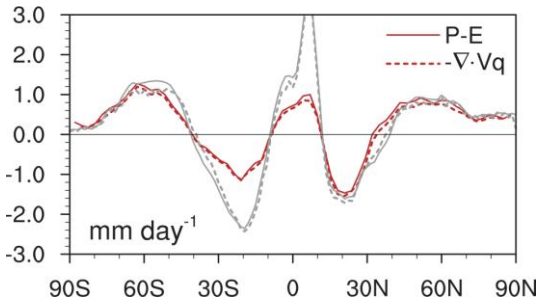

Fig.2 Hydrological cycle in the idealized model and observations. Zonal mean *P-E* (precipitation minus evaporation; solid line; mm day^{-1}) and horizontal convergence of moisture transport (dotted line; mm day^{-1}) in Ctrl run (red lines) and ERAI (gray lines) are shown.

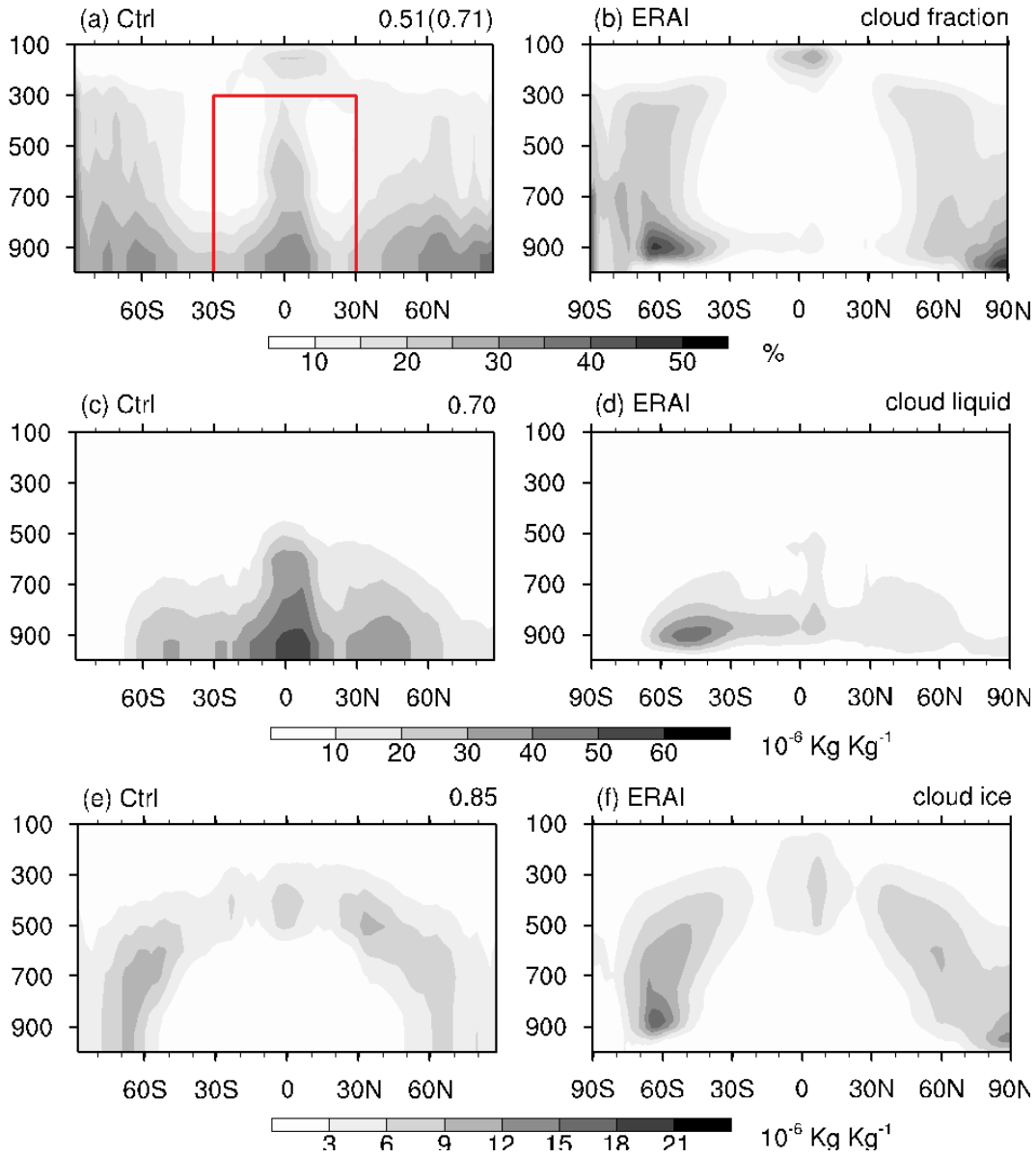

Fig.3 Clouds in the idealized model and observations. (a-b) Cloud fraction (%), (c-d) cloud liquid (10^{-6} kg kg^{-1}), (e-f) cloud ice (10^{-6} kg kg^{-1}) simulated in control run and that in ERAI. Weighted centered pattern correlation coefficients between the Ctrl and ERAI are shown at the upright of (a, c, d) for corresponding variables. The red box in (a) marks the tropical middle-low level clouds produced in this idealized model due to the lack of convection parameterization. The correlation coefficient in the brackets in (a) shows the pattern correlation with the exclusion of the red box region.

927

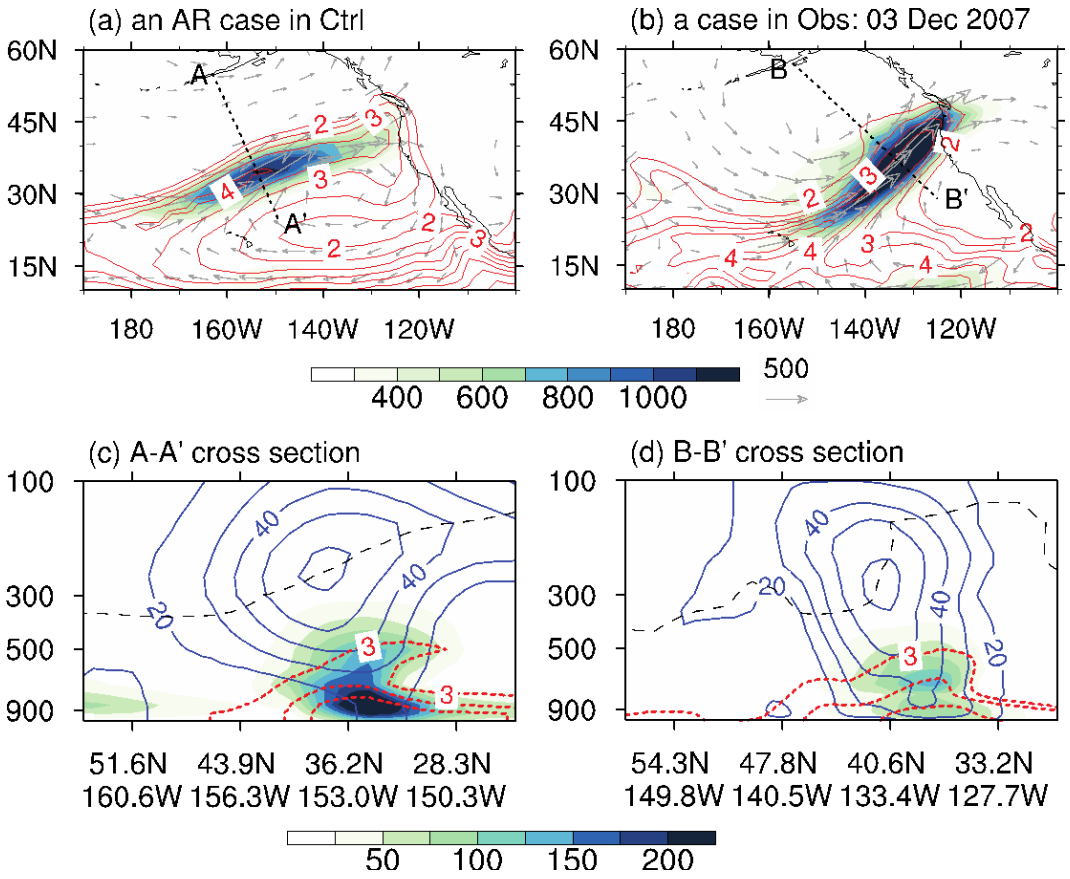

928

929 Fig.4 An AR case simulated in Ctrl run and a case in observation (ERAI), respectively. (a-b)
930 Integrated water vapor transport (IVT; kg m^{-1} s^{-1}) vectors (gray arrows; not shown if the
931 magnitude is smaller than 100 kg m^{-1} s^{-1}) and its magnitude (color shading), and integrated
932 water vapor (IWV; red contours; cm) in Ctrl (a) and ERAI (b). The position of the cross-
933 sections shown in (c-d) is denoted by the dotted line A-A' in (a) and B-B' in (b), respectively.
934 (c-d) Vertical cross-section perspective, including the core of the water vapor transport in the
935 atmospheric river (color shading), water vapor mixing ratio (red dotted lines; g kg^{-1}) and
936 cross-section isotachs (blue contours; m s^{-1}) in Ctrl (c) and ERAI (d). The tropopause is
937 denoted by the black dashed line in (c-d).

938

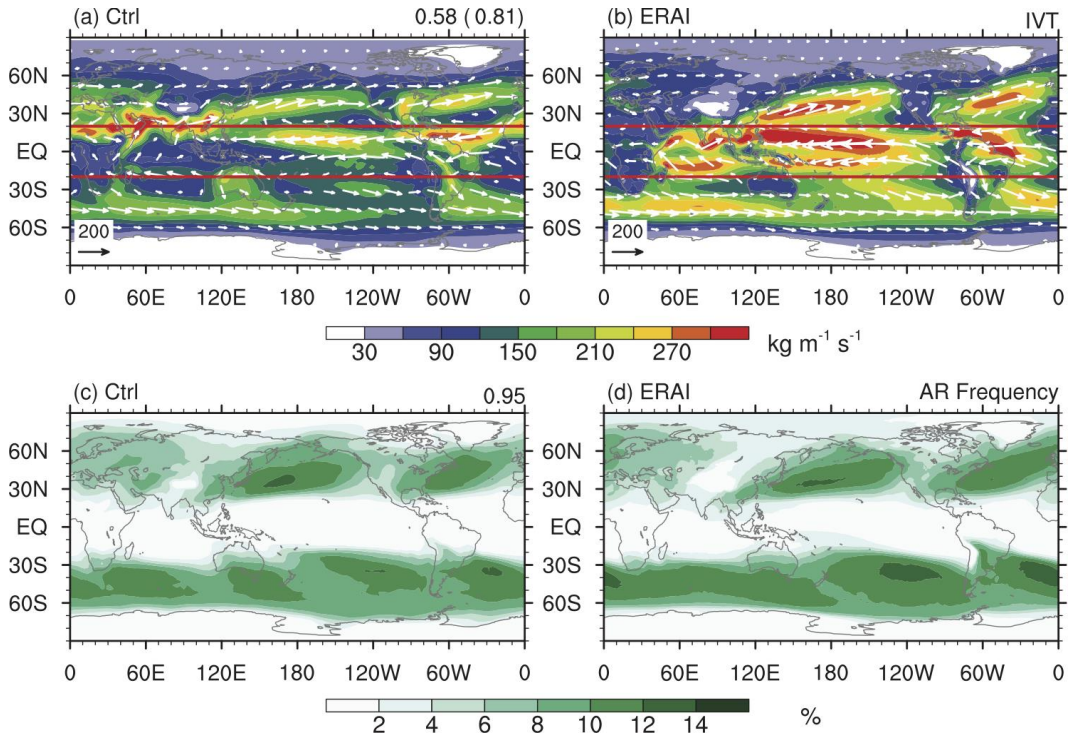

Fig.5 Mean integrated water vapor transport (IVT; kg m^{-1} s^{-1}) vector (white arrows) in Ctrl run (a) and ERAI (b). (c-d) same as (a-b) but for atmospheric river (AR) frequency (%). Weighted centered pattern correlation coefficients between the Ctrl and ERAI are shown at the upright of (a, c) for corresponding variables. The correlation coefficient in the brackets in (a) shows the pattern correlation excluding the tropical region (20°*S*-20°*N*; denoted by the red lines).

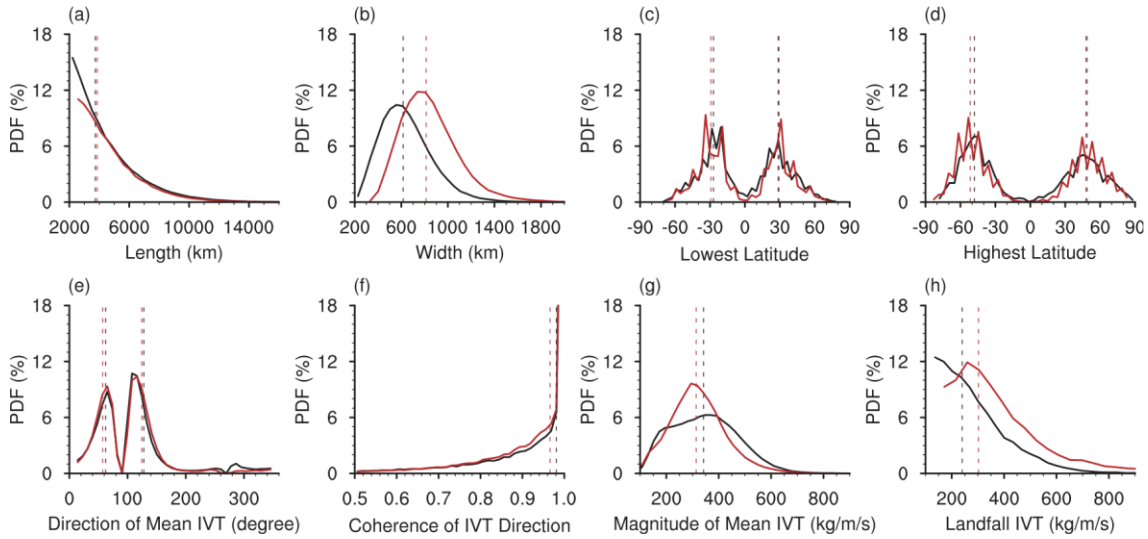

947

948 Fig. 6 PDFs of the basic characteristics of ARs in Ctrl run (red) and ERAI (black). (a) Length
949 of ARs. (b) Width of ARs. (c) Latitude of equatorward tip. (d) Latitude of poleward tip. (e)
950 Direction of mean IVT. (f) Coherence of IVT direction. (g) Magnitude of mean IVT. (h)
951 Magnitude of landfall IVT. The dashed vertical lines in each panel denote the median (in
952 case of one red line and one black line) or the median in each hemisphere (in case of two red
953 lines and two black lines) in Ctrl and ERAI, respectively.

954

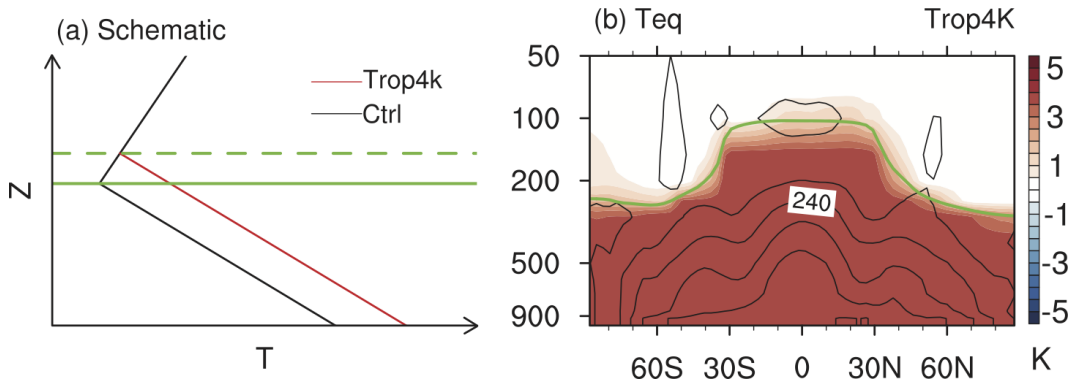

Fig.7 Design of uniform tropospheric warming forcing. (a) Schematic diagram for the changes to the vertical profile of tropospheric temperature due to global warming. Black line is an idealized profile of temperature in the troposphere and lower stratosphere. Red line denotes a uniform warming in the troposphere. Solid and dashed green lines in (a) denote the tropopause and its elevation due to the tropospheric warming forcing. (b) Equilibrium temperature (T_{eq}, units: K) in Ctrl (contour) and the 4K uniform tropospheric warming in T_{eq} for the Trop4K run (color shading). Green line shows the position of the tropopause in Ctrl. The forcings for Trop2K, Torp-2K and Trop-4K experiments were implemented in the model in a similar way.

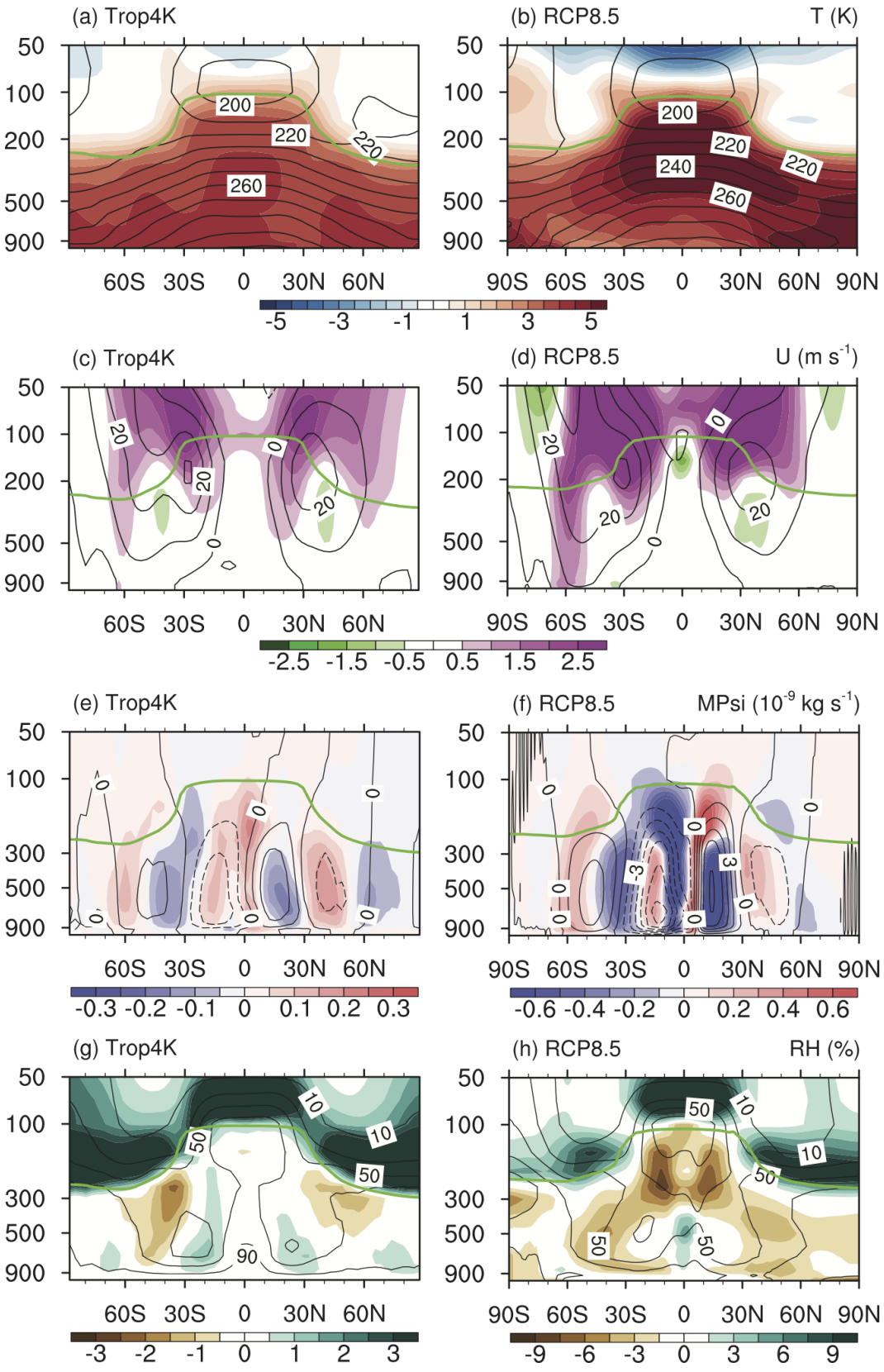

966

967 Fig. 8 Response of zonal mean temperature, zonal wind, meridional stream function and

968 relative humidity in the Trop4K run (left column) and RCP8.5 in CESM LENS (right
969 column). The contours denote the corresponding variables in Ctrl run (left column) and
970 historical simulations in CESM LENS (right column). Green lines denote the tropopause in
971 their reference states, respectively.
972

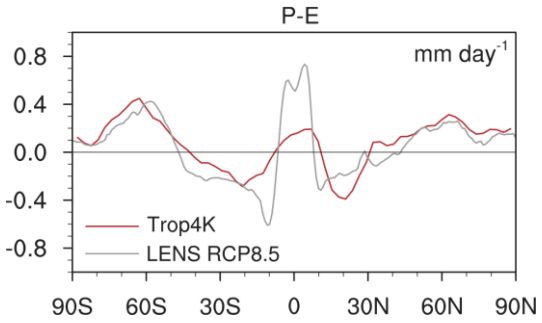

973

974 Fig. 9 Responses of *P-E* in the Trop4K run (red line) and CESM LENS RCP8.5 (gray line).

975

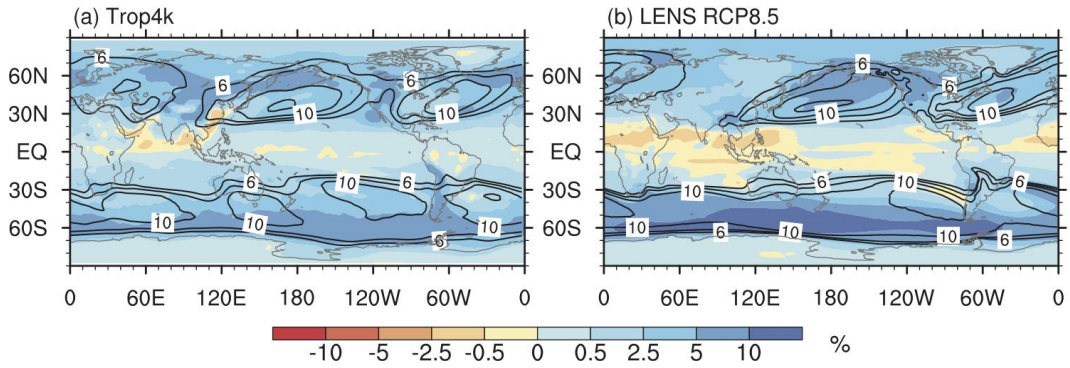

976

977 Fig.10 Frequency changes of Atmospheric Rivers in response to global warming. (a) AR
978 frequency (%) in Ctrl (contour) and its response (Trop4k-Ctrl) in Trop4K run (color shading).
979 (b) AR frequency in historical runs of CESM LENS during 1979-2005 (contour) and its
980 response in RCP8.5 runs during 2074-2100 (color shading).

981

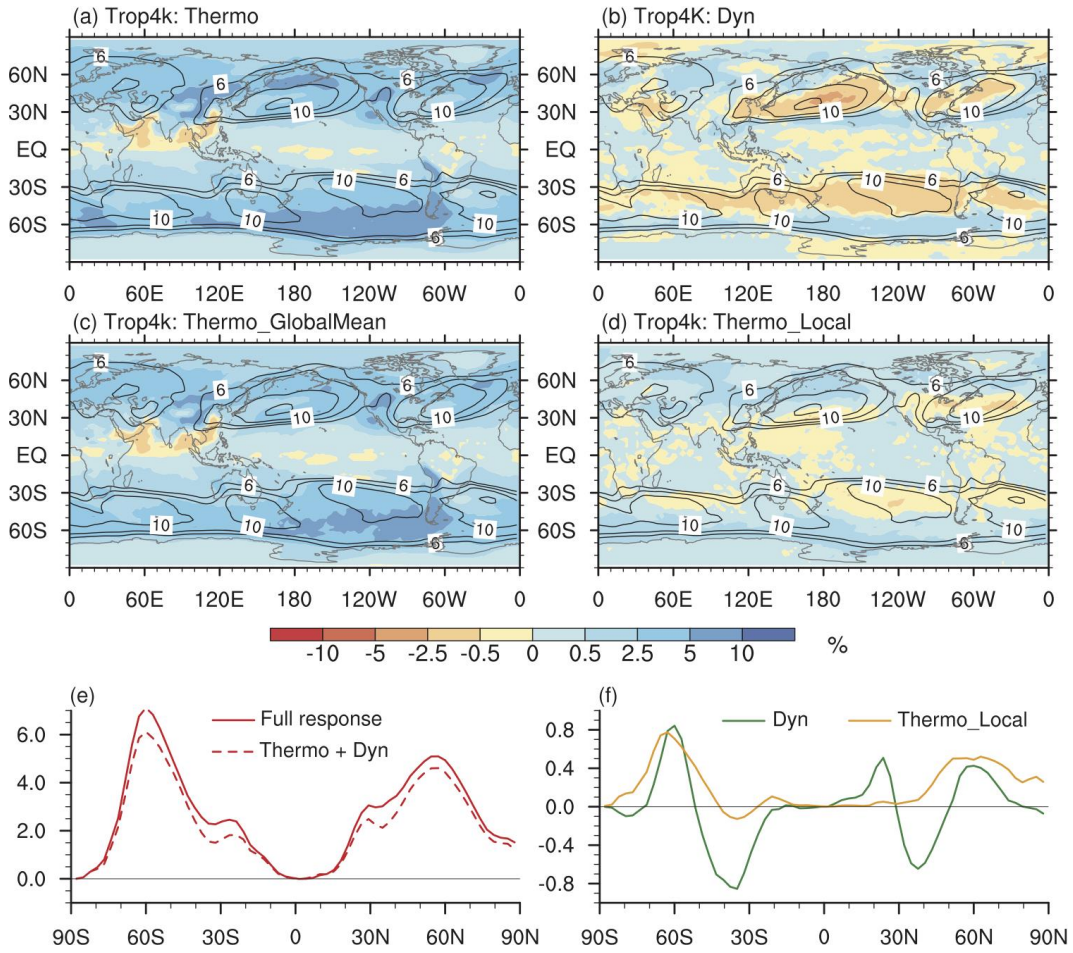

Fig.11 Decomposition of the response in AR frequency in Trop4K simulation. (a) Thermodynamic effect. (b) Dynamic effect. (c) Thermodynamic effect due to global mean warming. (d) Thermodynamic response due to local effect. (e) Full response and the sum of the thermodynamic and dynamic effects in zonal mean AR frequency. (f) Thermo_Local and dynamic effects in zonal mean AR frequency.

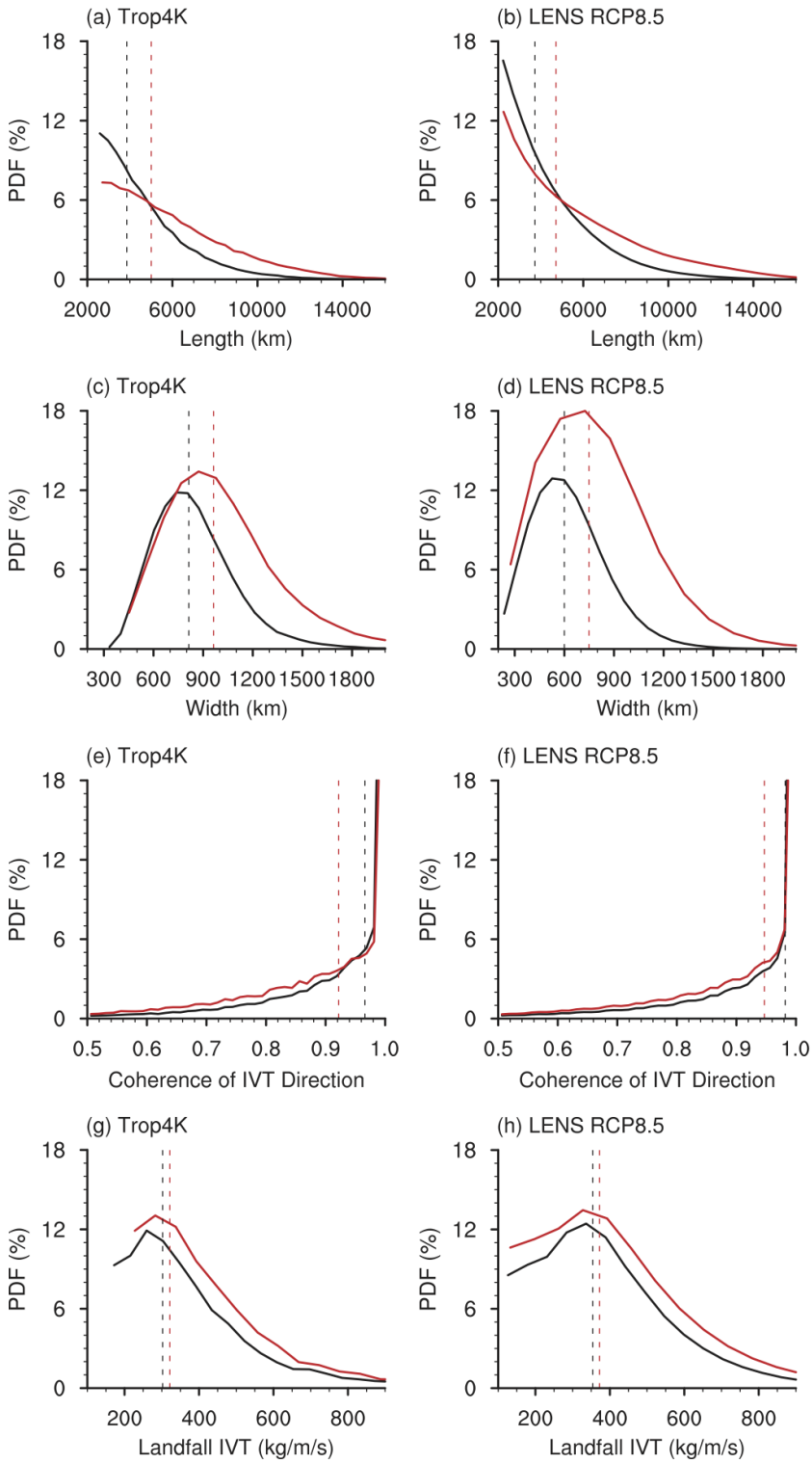

Fig. 12 Responses in the PDFs of AR characteristics to global warming in idealized model experiments (left) and CESM LENS outputs (right). (a-b) Length of ARs. (c-d) Width of ARs. (e-f) Coherence of IVT direction of ARs. (g-h) Magnitude of IVT at the landfalling point.

993 Black indicates the reference state (Ctrl or Hist) and red indicates the warmer climate
994 (Trop4K or RCP8.5). The two dashed vertical lines in each panel denote the median.
995

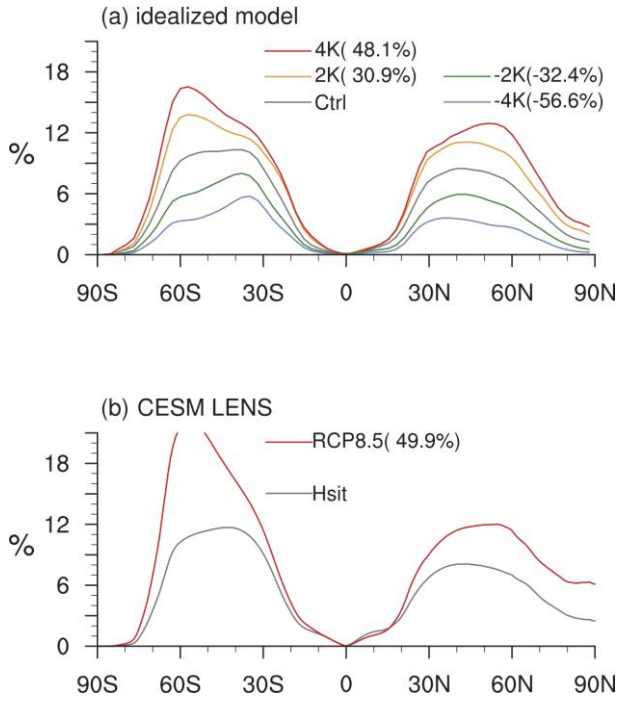

996

997 Fig.13 (a) Zonal mean of AR frequency (%) among a range of climates in idealized
998 simulations. The AR frequency changes relative to the Ctrl run are shown in legend (the
999 percentages, calculated as changes divided by reference state). (b) Same as (a) but for that in
1000 CESM LENS. For the tropospheric temperature response in CESM LENS, there is about
1001 4.4K warming in 2074-2100 in RCP8.5 runs compared to 1979-2005 in historical runs.

1002

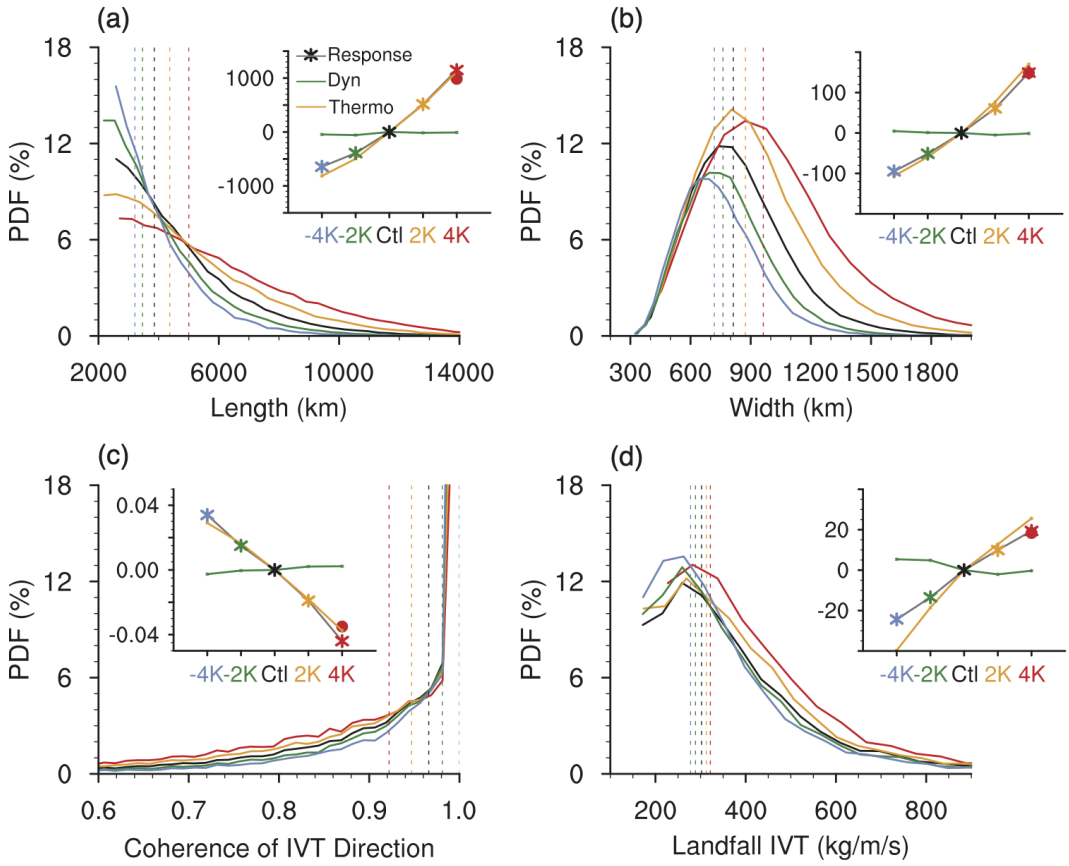

Fig.14 Same as Fig.11 but for that in Trop-4K (blue), Trop-2K (green), Ctrl (black), Trop2K (orange) and Trop4K (red) experiments. The line with colored stars in the line charts in every panel shows the median changes in sensitivity experiments, respectively. The green line and orange line in the line charts in each panel show the median changes in dynamic response and thermodynamic response, respectively. The median changes for each variable are defined as the differences between the medians in the 5 experiments and the Ctrl. The median changes with a 4.4K warming in RCP8.5 compared to HIST in CESM LENS are marked as red solid circles in the line charts.

1013 Table 1 Model experiments conducted in this study

	Exp name	Description
1	Trop4K	Forced by an additional uniform 4K warming in the troposphere
2	Trop2K	Same as Trop4K but with a 2K forcing
3	Ctrl	Control run
4	Trop-2K	Same as Trop4K but with a -2K forcing
5	Trop-4K	Same as Trop4K but with a -4K forcing

1014
1015